SANDIA REPORT

SAND2013-7921
Unlimited Release
Printed September, 2013

Bubble Masks for Time-Encoded Imaging of Fast Neutrons

Erik Brubaker, James Brennan, Peter Marleau, Aaron Nowack, John Steele, Melinda D. Sweany, Daniel Throckmorton

Prepared by
Sandia National Laboratories
Albuquerque, New Mexico 87185 and Livermore, California 94550

Sandia National Laboratories is a multi-program laboratory managed and operated by Sandia Corporation, a wholly owned subsidiary of Lockheed Martin Corporation, for the U.S. Department of Energy's National Nuclear Security Administration under contract DE-AC04-94AL85000.

Approved for public release; further dissemination unlimited.

Sandia National Laboratories

Issued by Sandia National Laboratories, operated for the United States Department of Energy by Sandia Corporation.

NOTICE: This report was prepared as an account of work sponsored by an agency of the United States Government. Neither the United States Government, nor any agency thereof, nor any of their employees, nor any of their contractors, subcontractors, or their employees, make any warranty, express or implied, or assume any legal liability or responsibility for the accuracy, completeness, or usefulness of any information, apparatus, product, or process disclosed, or represent that its use would not infringe privately owned rights. Reference herein to any specific commercial product, process, or service by trade name, trademark, manufacturer, or otherwise, does not necessarily constitute or imply its endorsement, recommendation, or favoring by the United States Government, any agency thereof, or any of their contractors or subcontractors. The views and opinions expressed herein do not necessarily state or reflect those of the United States Government, any agency thereof, or any of their contractors.

Printed in the United States of America. This report has been reproduced directly from the best available copy.

Available to DOE and DOE contractors from
U.S. Department of Energy
Office of Scientific and Technical Information
P.O. Box 62
Oak Ridge, TN 37831

Telephone: (865) 576-8401
Facsimile: (865) 576-5728
E-Mail: reports@adonis.osti.gov
Online ordering: http://www.osti.gov/bridge

Available to the public from
U.S. Department of Commerce
National Technical Information Service
5285 Port Royal Rd
Springfield, VA 22161

Telephone: (800) 553-6847
Facsimile: (703) 605-6900
E-Mail: orders@ntis.fedworld.gov
Online ordering: http://www.ntis.gov/help/ordermethods.asp?loc=7-4-0#online

SAND2013-7921
Unlimited Release
Printed September, 2013

Bubble Masks for Time-Encoded Imaging of Fast Neutrons

Erik Brubaker James Brennan Peter Marleau Aaron Nowack
John Steele Melinda D. Sweany Daniel Throckmorton

Abstract

Time-encoded imaging is an approach to directional radiation detection that is being developed at SNL with a focus on fast neutron directional detection. In this technique, a time modulation of a detected neutron signal is induced—typically, a moving mask that attenuates neutrons with a time structure that depends on the source position. An important challenge in time-encoded imaging is to develop high-resolution two-dimensional imaging capabilities; building a mechanically moving high-resolution mask presents challenges both theoretical and technical. We have investigated an alternative to mechanical masks that replaces the solid mask with a liquid such as mineral oil. Instead of fixed blocks of solid material that move in pre-defined patterns, the oil is contained in tubing structures, and carefully introduced air gaps—bubbles—propagate through the tubing, generating moving patterns of oil mask elements and air apertures. Compared to current moving-mask techniques, the bubble mask is simple, since mechanical motion is replaced by gravity-driven bubble propagation; it is flexible, since arbitrary bubble patterns can be generated by a software-controlled valve actuator; and it is potentially high performance, since the tubing and bubble size can be tuned for high-resolution imaging requirements. We have built and tested various single-tube mask elements, and will present results on bubble introduction and propagation as a function of tubing size and cross-sectional shape; real-time bubble position tracking; neutron source imaging tests; and reconstruction techniques demonstrated on simple test data as well as a simulated full detector system.

Acknowledgment

This work was funded under LDRD Project Number 165680 and Title “Bubble Masks for Time-Encoded Imaging of Fast Neutrons”.

Contents

1 Introduction **11**

2 Bubble Characteristics **13**

Initial Design and Testing 13

Other Tube Designs 18

Helical Mask 21

Controlled Fluid Flow 22

3 Simulations **25**

Description 25

Results 25

One-Dimensional Tube Geometry 26

Two-Dimensional Tube Geometry 29

Two-Dimensional Annulus Geometry 29

4 1D Bubble Mask Experiments **33**

Bubble Position Tracking Approaches 33

Experimental Setup 35

Combining bubble tracking and radiation detection 36

USB camera 38

Neutron detector setup 41

Arduino setup 42

Data collection run 00 44

5 Conclusion **57**

References **58**

List of Figures

2.1 Line drawing of initial test configuration 13

2.2 Bubble charateristics. 14

2.3 A 2 in ID mask tube that uses a side inlet port 16

2.4 An example of the shearing and distortion introduced by the rigid side inlet design 17

2.5 The bottom of the bubble is perturbed when using high pressure air and a short pulse width 18

2.6 Using a longer pulse duration and lower air pressure produced a very well defined and reproducible bubble 19

2.7 A bubble formed in the mineral oil filled tube 19

2.8 A bubble transiting up the tube filled with glycerine 20

2.9 Concept for a bubble mask detector 20

2.10 Conceptual helical mask 21

2.11 Helical mask with mineral oil and air injected 22

3.1 The simulated two-dimensional tube geometry 26

3.2 A one-dimensional simulated bubble mask 27

3.3 One-dimensional simulated reconstructed source positions 27

3.4 Two-dimensional reconstruction of a circular source, tube geometry 28

3.5 Two-dimensional reconstruction of a circular source, annulus geometry 28

3.6 Multi-point source reconstruction with no background 30

3.7 Multi-point source reconstruction with background, masked compared to unmasked 30

3.8 Multi-point source reconstruction with background, 13.5 cm thick annulus compared with 4.5 cm 31

4.1 Bubble tracking method 1 34

4.2 Bubble tracking method 2 35

4.3 Experimental setup 36

4.4 Amplitude and pulse shape discrimination for 1D setup 37

4.5 Neutron counts in experimental 1D setup 37

4.6 Photo of PC screen showing an entire USB cam frame and the text information, ROI box and aiming line placed on it using OpenCV functions. 39

4.7 Photo of PC screen showing the real-time analysis of the bubble ROI. 40

4.8 Full USB camera resolution bubble tracking data (top) and the same downsampled, inverted and aligned to create mask vector used by source position reconstructor (bottom). 40

4.9 Histogram of USB camera inter-frame time as measured by high-precision CPU timer. 42

4.10 Calibration using a ^{137}Cs source. Left: amplitude vs. pulse shape. Right: minimum and maximum ADC values. 43

4.11 Neutron source amplitude vs. pulse shape response. 43

4.12 Data run 00 experimental configuration. 44

4.13 Periodic bubbles, no source. 46

4.14 Periodic bubbles, AmBe source, $z = 0$ cm. 47

4.15 Semi-random bubbles, no source. 48

4.16 Semi-random bubbles, AmBe source, $z = 0$ cm. 49

4.17 Data run 01 experimental configuration. 50

4.18 Random bubbles, AmBe source, $z = -15$ cm. 51

4.19 AmBe source, $z = -15$ cm (left), $z = 0$ cm (center), $z = +10$ cm (right); 7 min. 52

4.20 Random bubbles, AmBe and ^{252}Cf sources, 5 min. 53

4.21 Two ^{252}Cf sources, 5 min. 53

4.22 Two ^{252}Cf sources, 5 min. 54

4.23 Two ^{252}Cf sources, 10 min. 54

4.24 Two ^{252}Cf sources, 60 min. 55

4.25 AmBe and ^{252}Cf sources, 60 min. 55

Chapter 1

Introduction

Fission-energy neutrons are an important signature of the special nuclear material (SNM) used in nuclear explosives, and high-resolution neutron imaging systems are desired for applications such as arms control treaty verification and emergency response. The time-encoded imaging technique produces images by inducing a time-dependent modulation of detected neutrons, and is characterized by simple and robust detector elements, low channel counts, and low cost, in contrast with other imaging approaches. However, time-encoded imaging of fast neutrons has never been demonstrated in a high-resolution mode needed for these applications. There are significant conceptual and engineering challenges in building a large high-resolution mask of bulky hydrogenous material, moving in a complex controlled fashion to produce the desired time-dependent attenuation patterns. We aim to enable high-resolution time-encoded imaging using the approach of bubble masks, in which arbitrary time-dependent neutron attenuation masks are formed by bubbles propagating through a viscous medium such as mineral oil.

Time-encoded imaging is an approach to directional radiation detection that is being developed at SNL with a focus on fast neutron directional detection [1]. Briefly, a time modulation of a detected neutron signal is induced—typically, a moving mask that attenuates neutrons with a time structure that depends on the source position. Time-encoded imaging is in many ways analogous to coded aperture imaging; the *spatial* modulation of a particle flux induced by a *fixed* mask on a *position-sensitive image plane* is replaced by the *time* modulation of a particle flux induced by a *moving* mask on one or a few *time-sensitive detectors*. An important unsolved challenge in time-encoded imaging is to develop high-resolution two-dimensional imaging capabilities; building a mechanically moving high-resolution mask presents challenges both theoretical and technical. For ideal imaging results using a uniformly redundant array (URA), a mask should produce the same attenuation pattern with different phase for different source positions in the field of view [2]. This is difficult to obtain in two dimensions for a simply moving solid mask. For example, a standard two-dimensional URA coded aperture mask, placed between a source and a detector and spinning on an axis through its center, does not produce a URA pattern in time.

We explored a potential technique that replaces the solid mask with a liquid such as mineral oil. Instead of fixed blocks of solid material that move in pre-defined patterns, the oil is contained in tubing structures, and carefully introduced air gaps—bubbles—propagate through the tubing, generating moving patterns of oil mask elements and air apertures.

Compared to current moving-mask techniques, the bubble mask is simple, since mechanical motion is replaced by gravity-driven bubble propagation; it is flexible, since arbitrary bubble patterns can be generated by a software-controlled valve actuator; and it is potentially high performance, since the tubing and bubble size can be tuned for high-resolution imaging requirements. Bubble masks could be a key enabling technology for high-resolution time-encoded imaging, with applications in arms control treaty verification and radiological emergency response. Bubbles can be introduced in such a way that a URA pattern moves through the tube(s) cyclically, satisfying the requirement for artifact-free image reconstruction in the ideal limit. In reality, for fast neutron imaging we cannot achieve the ideal conditions of full mask opacity, negligible mask thickness, far-field sources, and so on. With further study and simulations, the optimal mask pattern may turn out to be something other than a cyclical URA; the greater flexibility of a bubble mask relative to a mechanical mask allows the exploration of a larger space of time-encoded masks. In fact, with a bubble mask, data can be acquired with different mask patterns in the same measurement, possibly reducing systematic reconstruction effects relative to the use of a single fixed mask pattern.

Since theoretical modeling of the bubble propagation would be quite complex (due to turbulence effects, etc.), and the cost of materials is low, we have taken an experimental approach to determining the feasibility of the bubble mask concept. We built test structures with a single tubing element and bubble introduction mechanism. We investigated the effect of host medium viscosity; the size, shape, and slope of the tubing; and the rate of bubble introduction, all of which can affect the bubble propagation. This work is described in Chap. 2. Simulations, detailed in Chap. 3, allowed us to evaluate the imaging capability given observed bubble propagation characteristics, without the expense of building and evaluating a full imaging system based on bubble masks. Finally, targeted experiments were performed to validate the simulation results and to demonstrate source detection and position reconstruction with a simple (one-dimensional) but complete laboratory setup. As an important part of the latter effort, we developed an optical method for measuring and recording bubble positions as a function of time for feedback to the image reconstruction algorithm. The experimental work is presented in Chap. 4.

Chapter 2

Bubble Characteristics

Initial Design and Testing

Using air bubbles in a volume of liquid as a mask for fast neutrons could provide a unique and innovative way to create and change masks for a variety of detectors. To test this concept, we decided a simple experimental path would yield the best results. Our initial design was inspired by an art exhibit by artist Bruce Shapiro. Mr. Shapiro designed multiple bubble displays that use small tubes to align bubbles in patterns, sometimes depicting faces of historical figures. After a few emails with Mr. Shapiro we had the basic idea of what he used in his displays. Although our design would be different, the basic concepts would remain the same: Pick a tube material and diameter, use mineral oil as our liquid, and inject compressed air into the tubes.

An illustration of the test system is depicted in Fig. 2.1. Our initial design consisted of a 1.5 in ID acrylic tube that is 2 ft long. We used a simple 24 V power supply to deliver DC power to the Asco solenoid valve mounted to a check valve on the bottom of the tube. A DG535 delivered the pulse signal to the valve, allowing us to control repetition rate and pulse duration. House compressed air was regulated through a Parker air pressure regulator to allow fine control of the air delivered to the valve. Mineral oil was poured in to the open top of the acrylic tube to a level of about 18 in.

As seen in Fig. 2.2, bubbles emerge from the bottom of the tube. As the solenoid valve closes, small bubbles that remain in the valve to tube connection slowly exit and trail the

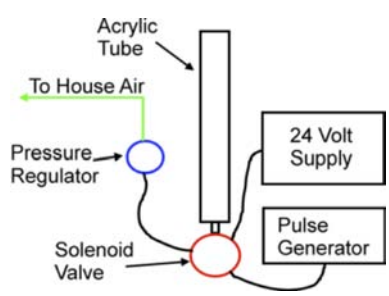

Figure 2.1. Line drawing of initial test configuration

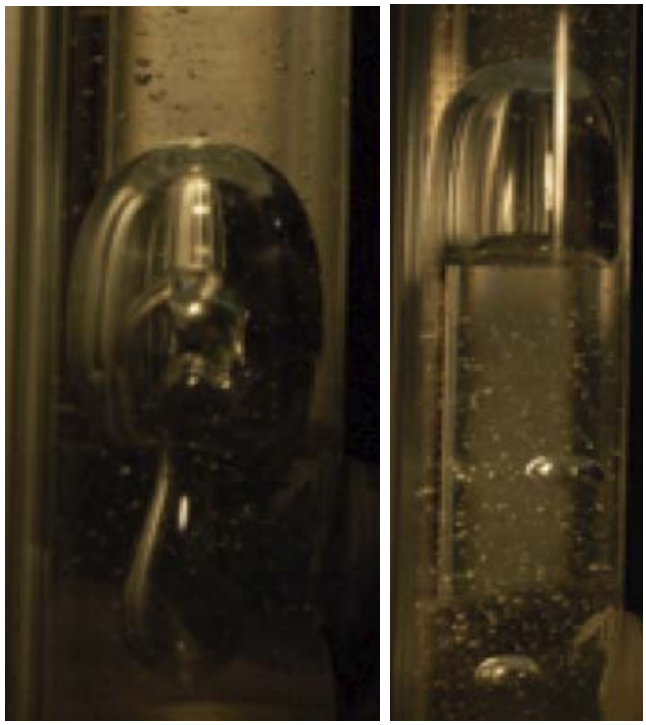

Figure 2.2. First image shows bubble as it emerges from the solenoid valve. Second image shows small after bubbles following the main bubble up the tube.

main bubble up the tube. These bubbles contribute additional small bubbles that remain in the mineral oil. Additionally, as the bubble size is increases the main bubble separates from the injection point as the buoyant force increases. This leads to multiple large bubbles being introduced into the tube instead of the desired single bubble. This problem keeps us from making larger bubbles and reduces the possible bubble configurations. While large bubbles are difficult to produce, smaller bubble sizes are very reproducible and transit up the tube at a very consistent velocity. If bubbles are introduced into the tube where the previous bubble is at minimum greater than one bubble length away from the subsequent bubble, the bubbles remain well separated. As an example, if the bubble introduced is 2 in long, as long as the next bubble isn't closer than 2 in from the previous they will remain separate. As the gap between the bubbles is decreased, there is a probability that the lower bubble will catch and combine with the previous bubble. This doesn't happen every time, but is undesirable because of the unpredictable nature of propagation.

Another issue that was discovered at this point was the effect of the bubble injection process. Using the fast open/close solenoid valve and the lower direct injection point creates a disruption to the previous bubble as the new bubble is injected. Often times breaking the previous bubble into multiple segments.as a new bubble is introduced into the tube the previous bubble is perturbed to the point of sometimes being broken apart. The new bubble

injected rapidly raises the column of mineral oil. This incompressible liquid hydraulically compresses and distorts the previous bubble. As pulse width and pressure is increased, the distortion of the previous bubble becomes more erratic. This sets an additional upper limit on bubble size. With this information in hand, we proceeded to test a few designs to help minimize or eliminate these issues. We now knew it was possible to create very consistent bubbles within a narrow scope. We sought to improve that with the following changes.

As the bubble is produced buoyant force causes the bubble to ascend. If the bubble is intended to be large it will break free from the inlet before the entire bubble has been formed. If the inlet is directly below the vertical mask element the bubble will form multiple rising portions. To combat this, we designed a tube that has a slightly ramped side inlet tube attached to the existing mask tube. This resembles a hockey stick, where the shaft of the stick is the mask tube portion and the heel of the stick is the inlet. This configuration allows a larger bubble to be formed. As stated earlier buoyant force works to separate the bubble from the inlet prior to its complete injection duration, the gradual slope of the slanted tube allows the bubble segments to recombine into the intended full size bubble prior to entering and ascending the main tube. This side inlet also serves as a buffer of mineral oil that can pass below the bubble being formed reducing the surge that affects the previously injected bubble. Since the newly injected bubble hugs the upper wall of the side inlet there is a large portion of the tube below the bubble that allows for the exchange of fluid from the front of the bubble to the rear. This reduces turbulence at the edge of the newly formed bubble allowing a smooth transition up the tube.

The next change was to place the injection port on the top of the side inlet tube. This change eliminated the small after bubbles that were present in the first test. In the first test the small volume of air that remained trapped in the pipe connecting the main vertical tube to the valve was the source of these bubbles. After the large bubble had formed and was ripped away by the buoyant force the small amount of air that remained behind in the valve tube slowly trickled out. This usually caused two small after bubbles to chase the main bubble up the mask tube. By moving the inlet location to the top of the tube, any air that didn?t exit with the main bubble injection would remain trapped in the inlet port. This eliminated all the small after bubbles.

The final change for this round was to replace the solenoid valve with a hose pinch solenoid valve. The original valve had a very rapid and abrupt opening and closing action. This action physically upset the tube and introduced additional shocks to any bubble already in the mask tube. The pinch valve used a foot to compress a length of tubing that effectively shuts off the air flow. This pinching action happens slower and can be adjusted by changing the durometer of the tubing in the valve. This provided a much smoother on/off transition. This slower air injection can be thought of as a wide Gaussian function compared to the Delta function of the previous valve.

These changes corrected the issues we had encountered in the first test design. When we tested this design we discovered a new issue that resulted from the rapid transition of the bubble from the side inlet to the main mask tube. As the bubble rounded the corner and started up the main tube the velocity of the mineral oil on the side opposite the inlet

Figure 2.3. A 2 in ID mask tube that uses a side inlet port.

Figure 2.4. An example of the shearing and distortion introduced by the rigid side inlet design.

tube was greater than that on the wall next to the tube. This caused some shearing and deformation of the bubble on the opposite side as it transitioned up the tube. You can see this in Fig. 2.4. To combat this abrupt transitional area, we changed from a rigid mask tube with an attached side inlet tube to a flexible tube. The flexible tube allowed us to make the side inlet tube transition into the main mask tube much more gradual. There was still a larger gap between the bubble and the wall on the opposite side which introduced a larger transfer of mineral oil on that side, but the overall impact was reduced to the point that the shearing and deformation of the bubble was almost completely removed.

With this new design producing consistent bubble shapes we began to investigate the production of different size bubbles. To produce different size bubbles either the air pressure or pulse width can be altered. We carefully studied the bubbles and adjusted the two parameters. Using high air pressure and a short pulse resulted in greater perturbation of the bubbles already in the mask tube. Figure 2.5 shows the impact on the bubble already transiting up the mask tube as the next bubble in injected. The bottom of the bubble is perturbed in a chaotic fashion. Next we tested a long pulse with lower air pressure. This resulted in a much more consistent bubble. Figure 2.6 illustrates this. Determining the exact air pressure and pulse width needed to produce the perfect bubble was an art form of twisting knobs and punching buttons until you got the bubble "just right." Since this wasn't strictly a bubble formation research project, once we landed on a set of parameters that gave us consistent and reproducible bubbles, we moved this design to the next phase of testing using radiation sources and video based bubble tracking.

The choice mineral oil was driven by the density of the liquid (~ 0.8 g/cm^3), the non-toxic

Figure 2.5. The bottom of the bubble is perturbed when using high pressure air and a short pulse width.

nature, and the easy compatibility with tubing materials. The bubble shapes produced were very consistent; however, there was some turbulence in the oil that caused a few anomalies in the bubble propagation. To investigate the impact of density on the overall bubble formation, we chose Glycerine as another "safe" liquid with higher density. Glycerine is non-toxic and has a density of ~ 1.26 g/cm^3.

Testing in the 1.5 in ID flexible hose showed distinct differences in the shape of the bubbles using these two liquids. Figure 2.7 and Fig. 2.8 show the bubbles formed using mineral oil and glycerine. The bubble shape in mineral oil has a convex top and a flat to concave bottom. The bubble is more prone to disturbance as the next bubble is injected. In the case of glycerine (Fig. 2.9), the bubble bottom is convex. Additionally, the bubble is less prone to disturbance as the next bubble is introduced which means the bubble shape remains consistent as it travels up the tube.

The more consistent bubble shape and transition up the tube when using glycerine encouraged us to use that configuration in subsequent testing with video bubble tracking and radiation source measurements. To add contrast for the video bubble tracking, blue dye was mixed into the glycerine solution.

Other Tube Designs

The conceptual design for a detector using bubbles and liquid as mask elements could look something like the image in Fig. 2.9. In this design a central detector is surrounded by tubes filled with liquid. Each tube could be independently controlled allowing various mask patterns to be produced in real time. In the case where a cylindrical mask is not ideal, one might want a square or rectangular tube cross-section. Our next step in mask design was to

Figure 2.6. Using a longer pulse duration and lower air pressure produced a very well defined and reproducible bubble.

Figure 2.7. A bubble formed in the mineral oil filled tube.

Figure 2.8. A bubble transiting up the tube filled with glycerine.

Figure 2.9. Concept for a bubble mask detector.

investigate this case.

We started with a simple 1 in x 1 in square tube with an internal wall dimension of 0.83 in per side. We took the lessons learned in the cylindrical tube tests and applied those design criteria to the square tube. Initial tests were performed using mineral oil as we knew we could get a good bubble. The use of mineral oil also allowed for easy transfer of liquid from design to design as it is a less sticky liquid.

Initial results showed similar performance of both bubble injection and propagation. Bubble shapes were very consistent from bubble to bubble. It was noted that the bubble had the same shape as those in the cylindrical tube. The desire was to have the bubble fill more of the tube, expanding into the corners if possible. This desire is driven by the need to have as little material between the radiation source and the detector when a bubble is present. Any additional material would further attenuate the neutron source, degrading

Figure 2.10. Conceptual helical mask.

performance. We experimented with larger bubble sizes and discovered an interesting effect. As we increased the bubble size, the bubble would expand towards the wall of the tube until it reached about 75% of the tube cross-section, then it would expand along the length of the tube. Adding more air at this point would only make the bubble longer in the longitudinal direction. The bubble does not expand towards the wall or fill the corner any more. Also noted was, as the bubble became very large (several cross-section lengths long), the fluid flow in the corners of the tube would begin to shear the sides of the bubble. This shearing caused long streamers of air to extend past the bottom of the bubble in the corners. This streaming of air was mixed with the mineral oil in the tube and began to infuse the oil with tiny bubbles that remained in the tube for extended periods of time.

Further testing was conducted using 1 in x 4 in and 2 in x 4 in interior cross-section tubes with similar observations. The bubble would expand to fill the tube to only about 75% and remain curved at the corners of the tube. In the case of the 1 in x 4 in tube, nearly 1 in of mineral oil and 0.25 in of acrylic would remain on the center line of the tube between a neutron source and the detector. This amount of material only increases as you approach the sides of the tube. This makes this configuration less than ideal for some detection scenarios.

Helical Mask

Another possible mask design could be a single tube of flexible material wrapped in a helix. This design could have advantages as there would only need to be one solenoid valve and the associated electronics would be simpler. Figure 2.10 shows a conceptual illustration of such a design.

To test this design we coiled a length of flexible tubing around a structural frame. A similar side injection port to those implemented in the previous designs was used. Mineral oil was again used as it provides similar results to that of glycerin while being easier to clean up after testing.

Figure 2.11. Helical mask with mineral oil and air injected.

We began injecting air into the helix and determined that this design was not going to be practical in this configuration. We had anticipated the bubble floating to the top of the tube as it gradually moved up the tube. What was not anticipated was the deformation of the bubbles as the next bubble was introduced. As can be seen in Fig. 2.11, a bubble is formed and sticks closely to the top of the helix. There are strongly curved features at the lead and trailing edges of the bubble. The bubble fills about 1/3 the volume of the tube at the maximum point. While this is not the ideal bubble shape, this could be a utilized with proper bubble tracking. The problem comes as the next bubble is injected. As the next bubble begins to fill the helix at the injection port, the previous bubbles stretch out along the top edge of the tube. The bubbles now only occupy a thin layer at the top of the tube, comprising about 5% of the tube volume along the cross-section. The bubbles also go through a chaotic surging from thin to thick, never staying in one form long enough to be of much use as a mask. While more work could be done to try and optimize this mask design, considering the scope of this project we determined that this design would be abandoned.

Controlled Fluid Flow

An observation made in the cylindrical and square tube designs was the impact fluid flow past the bubbles had on their shape and propagation. To further study the effects of this flow past the bubble, we decided to move liquid through the tube as well as inject bubbles. The goal was to examine if the bubble could be encouraged to fill a larger volume of the tube with respect to the cross-section. In addition, possibly this flow could change the overall shape of the ends from concave/convex to a more square profile.

In this system, a peristaltic pump was used to move fluid from a holding reservoir through the tubing. Along the input line, bubbles were injected into the flow of mineral oil. Side by side tests were performed to visualize if any changes could be seen in the bubble formation or propagation. In the end, the bubble geometry and propagation were unchanged. However, even though the bubble didn't change, there is a possible advantage to using forced fluid flow in the tube. As discussed earlier, when the bubbles are injected, the fluid in the tube is forced upward as the expanding gas displaces volume. This displacement causes the bubbles

already in the tube to jump up slightly as they are carried by the flow. The force of this jump was minimized by going to the pinch solenoid valve, but the net displacement remained the same. The previous piston style solenoid caused a rapid jump to the full displacement value and this rapid jump caused massive perturbations in larger bubbles. By using fluid flow through the tube, one could adjust the flow to compensate for this jump by flowing liquid between injections of air. For clarity, as the air is being injected, fluid flow would be minimized or stopped. Once the air injection begins to taper off, fluid flow would ramp up to keep the net displacement of fluid constant. While video tracking (discussed in the following sections) can compensate for rapid changes in the bubble positions, minimizing the displacement and smoothing out the flow would be very useful.

Of particular interest was the effect of tube inside diameter. As the tube ID was decreased and positive flow from the pump was used, the bubbles became locked to the wall. As the tube ID increased, the bubbles became free from the wall and mineral oil would form a layer between the wall and the bubble. In the ideal case, there would be no liquid between the wall and the bubble. Again, the least amount of material between the source and the detector is desired. When tube sizes were ~ 0.375 in, bubbles could be pumped backwards down the tube against the buoyant force. In an application where the mask elements could be optimized around a small size, flowing bubbles against the buoyant force could offer new possibilities for mask patterns and bubble control. We demonstrated that we could move bubbles down, stop perceived flow, and let them rise slowly. This level of control is unique to this type of dynamic mask.

Chapter 3

Simulations

The simulation of time-varying bubbles propagating in a fluid presents a unique problem: depending on the various factors, most notably the size of the bubble, the propagation speed varies bubble by bubble, and is often not constant for a given bubble throughout the length of the tube. However, in order to reconstruct the position of a neutron source, the position and size of each bubble must be known. This information is obtained in real time with a web-camera, discussed further in Chap. 4, and then passed to a routine which calculates the response to the given bubble mask at a particular frame, then reconstructs the neutron source position.

Description

The detector geometry is first modeled using the ROOT data analysis package: the detector and tube are constructed with the proper material properties, and the tube is broken up into cylindrical voxels. A source space in (ϕ, z) is also defined at a given radius away from the tube. Figure 3.1 is a rendering of one geometry simulated, in which the mask is a series of tubes arranged in a circle around one detector: the tubes are 4.48 cm in diameter, chosen to be the neutron attenuation length through water.

For a given source position, the distance passing through each voxel is then calculated for a several hundred random trajectories starting at the detector and ending at the source position. The average attenuation length for each voxel and source position is then used to calculate the total attenuation for a given trajectory and arbitrary bubble mask. Depending on whether a given voxel is filled with water or air, the individual voxel attenuation lengths are summed and used to determine the response for a given source position and mask. In this way, the detector response can be calculated in real time, so long as the bubble mask is passed to the simulation routine. The source is reconstructed using a Maximum Likelihood Expectation Maximization (MLEM) algorithm [3].

Results

Three different geometries are constructed to test the validity of a bubble mask. A 1-dimensional source space with one vertical bubble mask was constructed in order to recon-

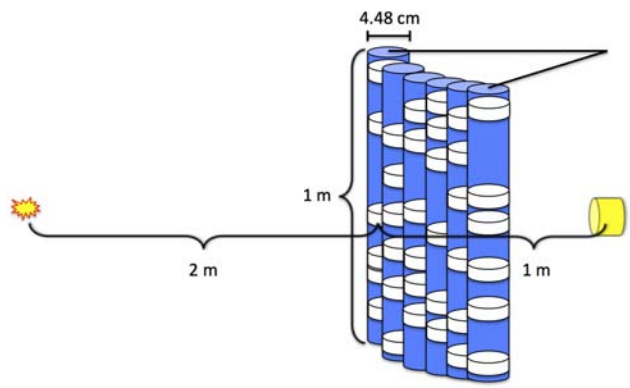

Figure 3.1. The simulated two dimensional tube geometry: the detector is at the center, the tube array is at a radius of one meter, and the source space is at a radius of 3 meters in reference to the detector. Each tube is 4.48 cm and one meter tall.

struct the position of sources in the data obtained from Chap. 4. The geometry in Fig. 3.1 was constructed as the most likely 2-dimensional extension of the current experimental setup. A third geometry was constructed as an open annulus to eliminate effects of non-uniform attenuation on the sides of tubes.

One-Dimensional Tube Geometry

A random bubble mask with an open fraction of approximately 50% was generated in one tube, where the minimum bubble and water height was 4 cm, and bubbles propagated at 10 cm/s regardless of size. Figure 3.2 shows a bubble mask for the entire length of a simulated data run: each cylinder voxel is either one or zero for a given time frame, indicating whether the voxel is filled with water or air respectively.

Several source geometries were input to test the reconstruction abilities. Figure 3.3 shows the reconstructed source position of a 10 min simulated data run, from left to right, for one point source, two point sources, and a line source. The red line indicates the true source positions, or in the case of the line source the linear extent of the line. In each case, the source strength is 10 Hz uniformly over the spatial extent: for example for two sources, each source has a rate of 5 Hz. There is no background field present. Finally, the MLEM algorithm goes through 300 iterations to determine the source position.

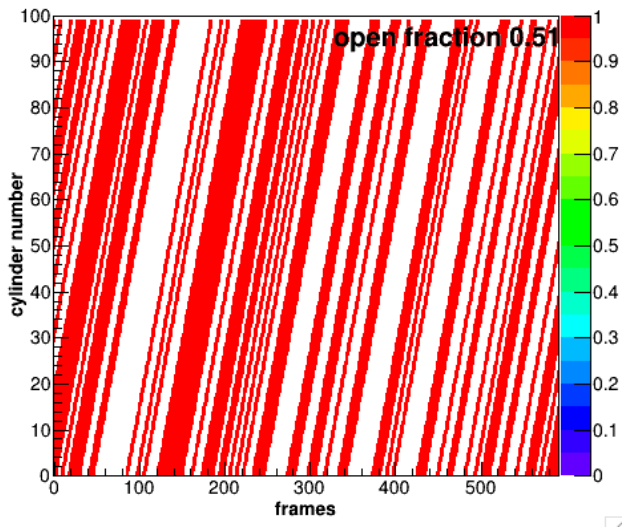

Figure 3.2. A one dimensional simulated bubble mask, with an open fraction of 51%. The air bubbles are zero or empty regions (white), and the water is in one or filled regions (red). The entire simulated data run, in this case 600 frames, is shown, and the tube is broken up into 100 cylindrical voxels.

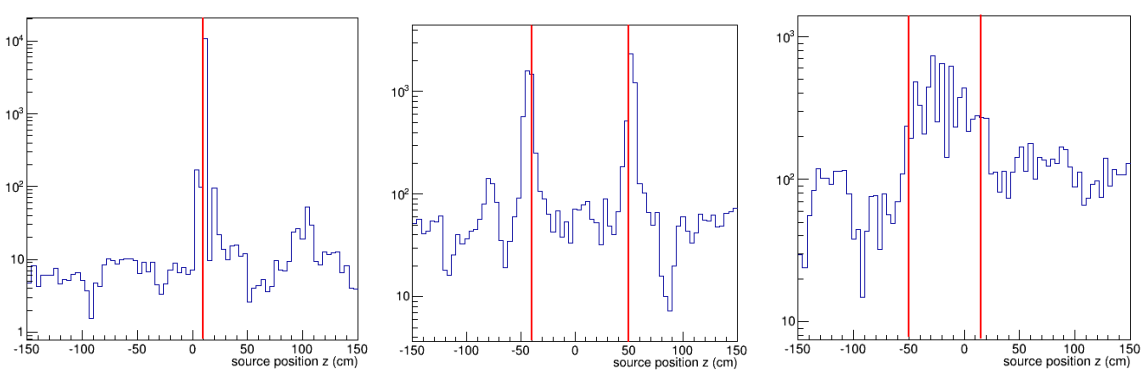

Figure 3.3. The reconstructed source positions for a one-dimensional bubble mask. From left to right: one point source at 10 cm, two point sources at −40 cm and 50 cm, and a line source extending from −50 cm to 15 cm. For each simulation the source strength is 10 Hz, and there is no background present. The MLEM algorithm has gone through 300 iterations.

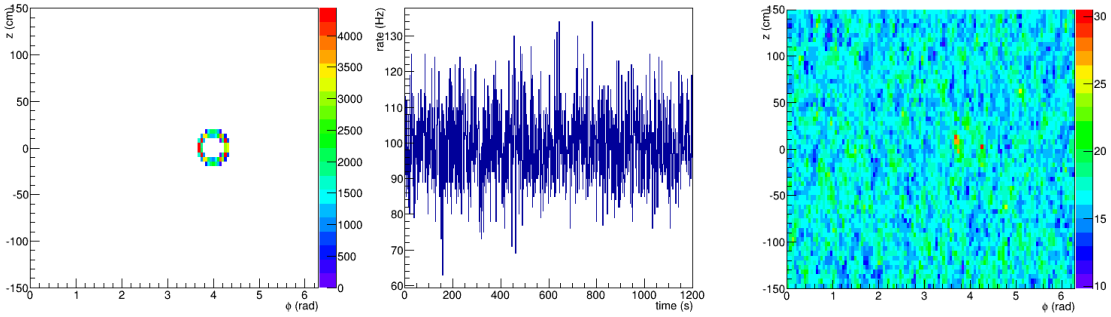

Figure 3.4. Two-dimensional reconstruction of a circular source with the tube geometry. The simulated data run was 20 min long, had no background, and the reconstruction used 500 MLEM iterations.

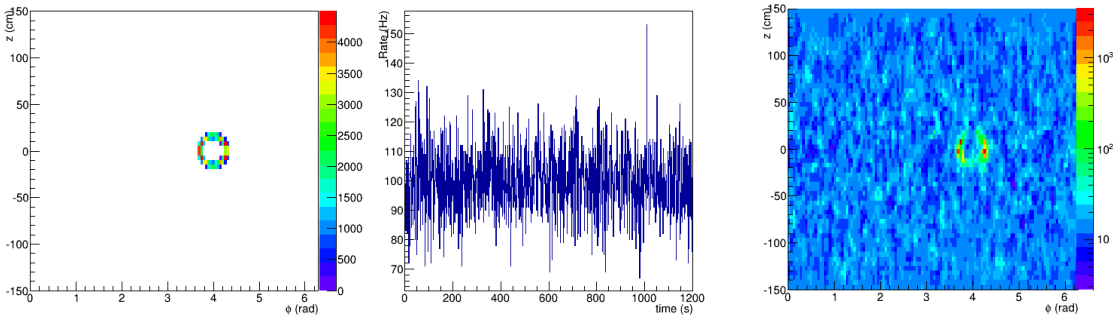

Figure 3.5. Two-dimensional reconstruction of a circular source with the annulus geometry. The simulated data run was 20 min long, had no background, and the reconstruction used 500 MLEM iterations.

Two-Dimensional Tube Geometry

Although the tube geometry is the most likely two-dimensional extension of our current experimental setup, it is not ideal because the area between tubes will have poor masking of neutron sources. The reconstruction of a circular source is demonstrated here as a direct comparison to the annulus geometry, to determine if the tube edges have any measurable effect on the reconstruction of sources.

Figure 3.4 is for a 100 Hz source and no background: the reconstruction on the right is not ideal with a significance of at most 3.9. The generated source distribution and detector rate are also shown. The identical parameters for the annulus geometry in Figure 3.5 reveals some differences , however the effects may be washed out because the binning width covers the circumference of a tube.

Two-Dimensional Annulus Geometry

One of the advantages to a bubble mask, as opposed to a stationary mask constructed of polyethylene, is that one can take full advance of the benefits of time-encoded imaging. There are several scenarios in which the mask pattern and open fraction can be changed to optimize the detection of particular sources. For example, in the case in which one very strong source is placed next to another weaker source and fully obscures it, the tubes contributing the greatest signal from the strong source could be changed to have a very small open fraction, or even entirely filled with water. Then, only neutrons from the weak source would have a high probability of interacting with the detector, making it easier to see. Another scenario which would benefit from this type of real-time masking is one in which the background is high and the source location is known, but details of the image are not: in this case, masking off all tubes except those in which the source contributes should yield a better image. One could look for features in the source by altering the open fraction iteratively over the known spatial extent of the source.

Figures 3.6 and 3.7 demonstrate the effect of masking the contribution of background. In Fig. 3.6, three source points, two with equal strength, and one approximately half the strength, are reconstructed with no background present. However, when background is added the reconstruction is less successful for the source at 5.5 radians: in Fig. 3.7, top right, there is little discernible contribution over background. However, when one masks the tubes in the $-150 < z < -50$ and $50 < z < 150$ range, as is done in the bottom right of Fig. 3.7, the source at 5.5 radians become visible over background.

Finally, a geometry with a 13.5 cm thick annulus was simulated: Figure 3.8 shows the reconstruction of the same three sources and background level compared with a 4.5 cm annulus. The acquisition time and MLEM iterations are the same: 20 min and 500 iterations. On the far right is a histogram of the reconstructed source rate for all bins: the improvement in the reconstruction is clear by the increased separation of the background peak and the values at the hot spots.

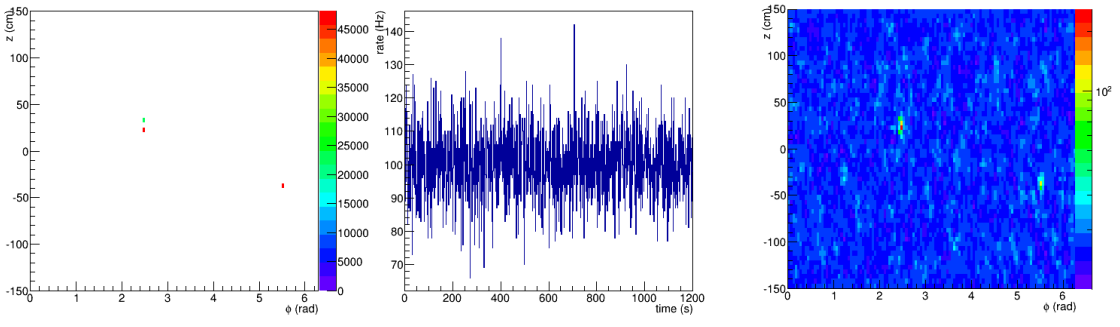

Figure 3.6. A multi-point source distribution with no background and differing source strengths, reconstructed with 500 MLEM iterations.

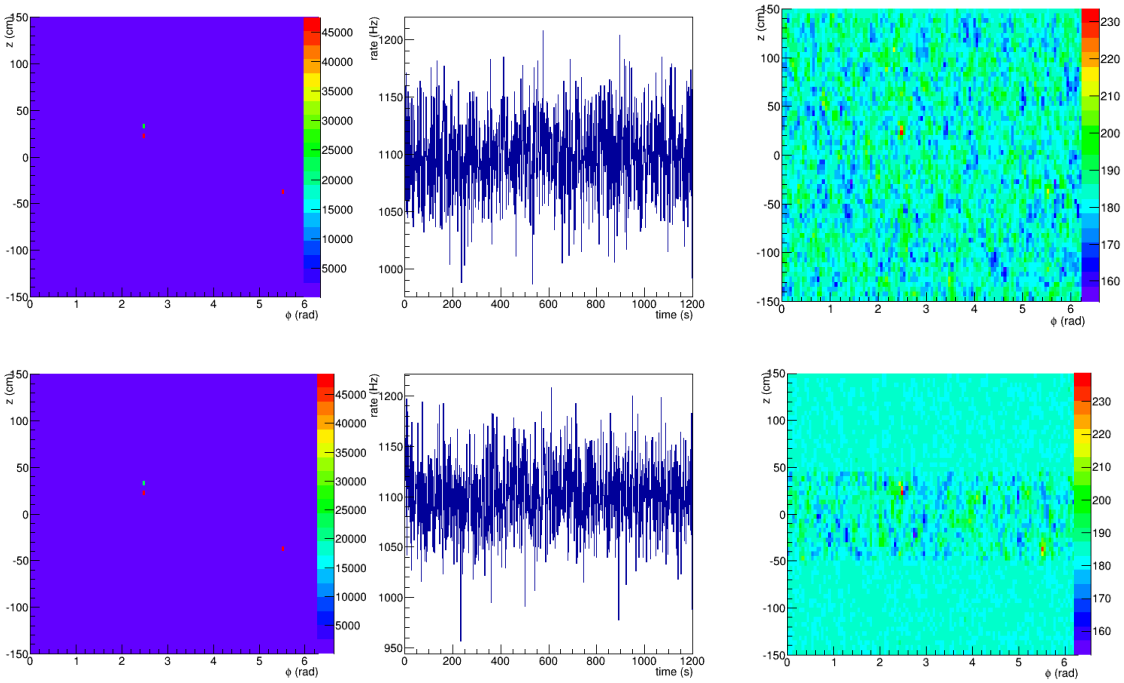

Figure 3.7. A multi-point source distribution with 1000 Hz uniform background, reconstructed with 500 MLEM iterations. For the bottom series of plots, the tube z positions ranging from $-150 < z < -50$ and $50 < z < 150$ have an open fraction of 2%, and the remaining, from $-50 < z < 50$ have an open fraction of 50%.

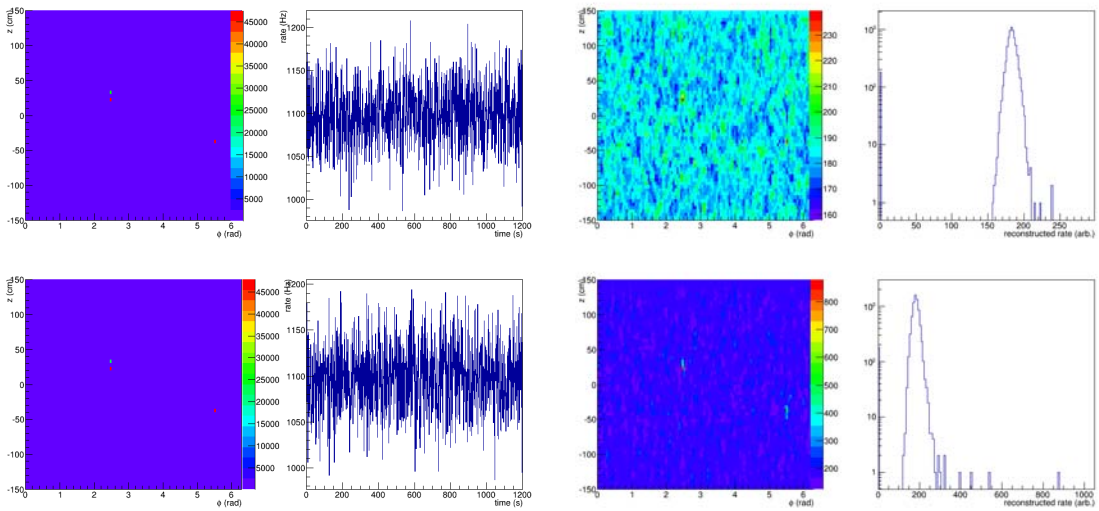

Figure 3.8. A multi-point source distribution with uniform background with an annulus 4.5 cm (top) and 13.5 cm (bottom) thick, reconstructed with 500 MLEM iterations. On the far right is a histogram of the reconstructed source rate for all bins: the improvement in the reconstruction is clear by the increased separation of the background peak and the values at the hot spots.

Although the geometries and scenarios presented here are not exhaustive, we have successfully developed a tool to test various geometries and scenarios in the future.

Chapter 4

1D Bubble Mask Experiments

Bubble Position Tracking Approaches

In order to reconstruct radiation sources the shape of the mask must be known at each time. This is done by tracking the position and shape of each bubble over a data run. While we have the information of when a bubble was injected into the tube and with how much air, it is not straightforward to extend that information to bubble size and position for a variety of tube shapes, liquids, and other conditions. Instead we acquire a video of the run and use techniques from the field of computer vision for measuring bubble position and size. Using the freely available OpenCV library [4], we developed a generic position tracking algorithm and a more specific and simple method. For this method, the OpenCV Python bindings were used to access its functionality.

The generic algorithm is based on measuring significant changes in time on a per-pixel basis. A running average of the past several frames is calculated and subtracted from the current frame. The resulting image only displays areas of motion within a frame, displayed as a green overlay in Fig. 4.1, left. These areas of motion are then surrounded by a bounding box. Any overlapping bounding boxes are expanded and then combined to group neighboring regions for a bubble. This results in the real-time object position tracking in Fig. 4.1, right. While this method works in a variety of cases and is able to track most bubbles it cannot tightly constrain the bubble due to the churning motion of the liquid that trails it. Also, the bounding boxes constantly adjust their size making it difficult to measure the center position of a bubble.

The next approach is simpler and is based on comparing the values of pixels within a region before bubbles are injected into the tube and afterwards. A box indicating the region of interest is made and calculations are restricted to this region. The pixels are averaged horizontally, resulting in an array of pixel values for each vertical position. This is done for the red, green, and blue (RGB) channels separately. A baseline array for each RGB channel is made by time-averaging this array over the period before bubbles are injected into the tube. Once bubbles are injected into the tube the baseline array is subtracted from the calculated array in the current frame. The bubbles are clearly visible as deviations above this value and a simple threshold on this difference tightly tracks each bubble as seen in Fig. 4.2, left. While this method is simpler it turned out to be more useful as the edges of

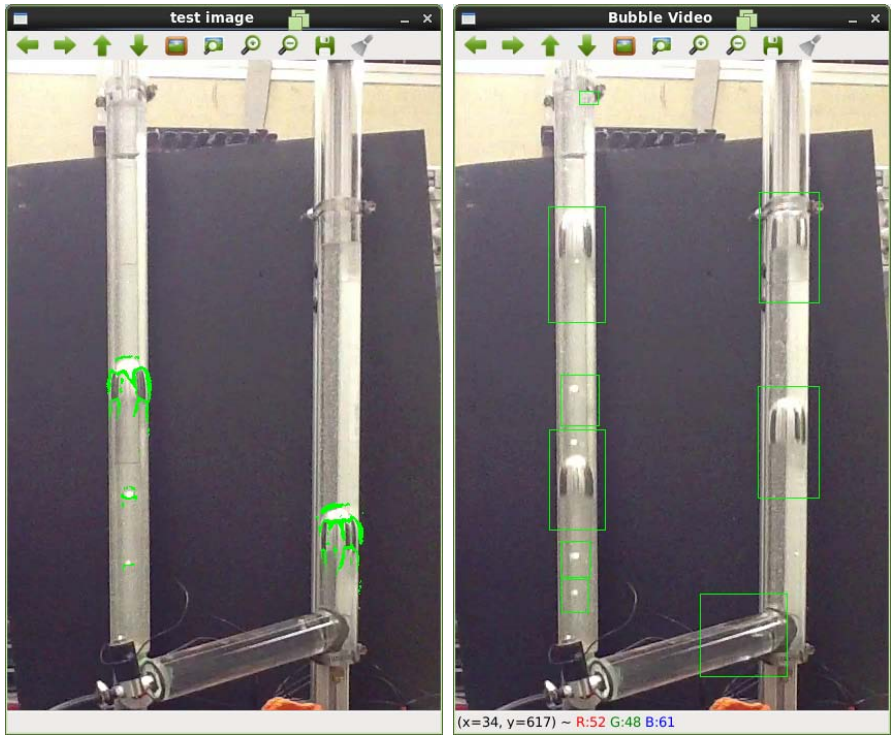

Figure 4.1. Left: the differences of the current frame compared to previous frames is overlaid in green. Right: the resulting bounding boxes for areas of motion.

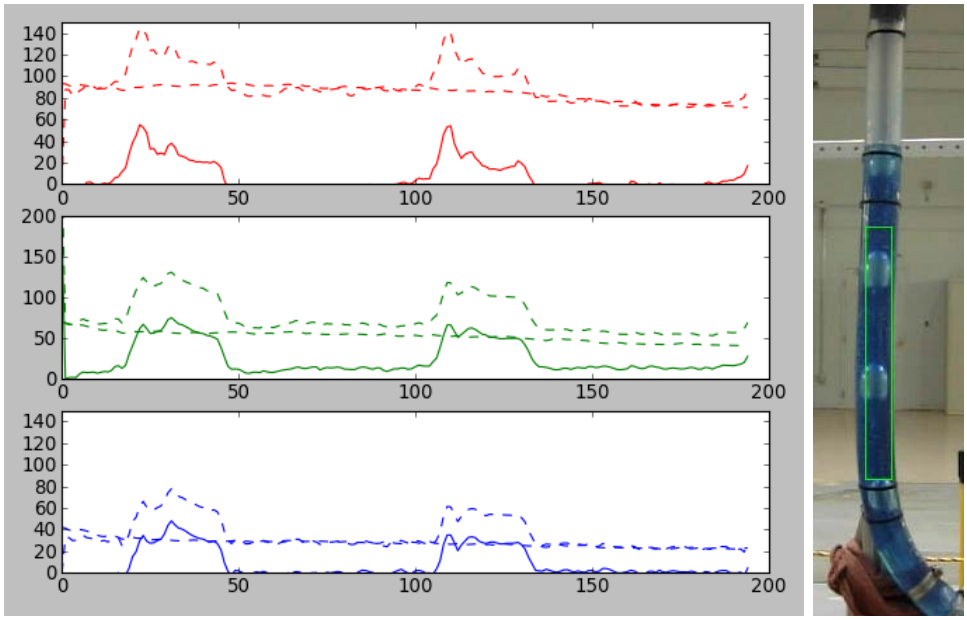

Figure 4.2. On the left the baseline and current vertical pixel values are shown (dashed) and the deviation from the baseline is show (solid). Right: The region of interest is overlaid on the image

the bubbles are clearly defined. This allows us to input an accurate mask into the source reconstruction algorithm.

Experimental Setup

The experimental setup, shown in Fig. 4.3, consists of a tube of colored glycerol with a source stand and a PMT on opposite ends. The PMT is coupled to a 1 in dia. x 1 in cylinder of liquid scintillator and full pulse waveforms are read out and saved for offline analysis. The bubbles are released through an air-pressure solenoid valve which is controlled through an Arduino UNO over usb to the data acquisition computer. An energy calibration dataset using a ^{22}Na source is used for converting the pulse integrals to electron-equivalent energy, shown in Fig. 4.4, left. Neutrons have a longer pulse length than gammas in liquid scintillator, so a pulse shape discrimination (PSD) parameter based on the ratio of the tail pulse integral to the total integral is used to select neutrons only. The PSD parameter vs pulse height is shown in Fig. 4.4 on the right, with the fit neutron and gamma discrimination fits overlaid for an AmBe source.

An early test was made to measure the effects on the neutron rate caused by propagating bubbles. A constant bubble shape is injected into the tube at a constant rate of 1 Hz for one

Figure 4.3. Experimental setup of the bubble acquisition system: a PMT is placed opposite of a source stand with the glycerol tube and bubbles placed in between

hour. By plotting the number of detected neutrons as a fraction of the bubble period, the average rate of neutrons for many bubbles can be calculated. The resulting plot in Fig. 4.5 shows that an air bubble allows at most 30% more neutrons to pass through to the detector for this tube and detector size.

Combining bubble tracking and radiation detection

In Sec. 4, the video bubble tracking and neutron detection data streams were acquired by two independent systems—an iPad as video recorder for the bubbles and a CAEN DT3720 USB desktop digitizer for the neutrons—and the above analyses consider interesting features inferred from each separately. These independent acquisition systems did not lend themselves readily to recovering the time relationship between the bubble positions and detected neutrons necessary to robust neutron source position reconstructions.

In order to combine the video and detector data, a new acquisition scheme was devised. This system used a Logitech C210 USB web cam to capture the bubble position images and a VME crate containing a Struck SIS33350 digitizer and an Iseg VHS3040n high voltage supply to capture the neutron detector response. The choice of these alternate data input sources allowed one program on one PC to synchronously receive data from each and store that data appropriately time-stamped in a single data file. Programs were written entirely using C++

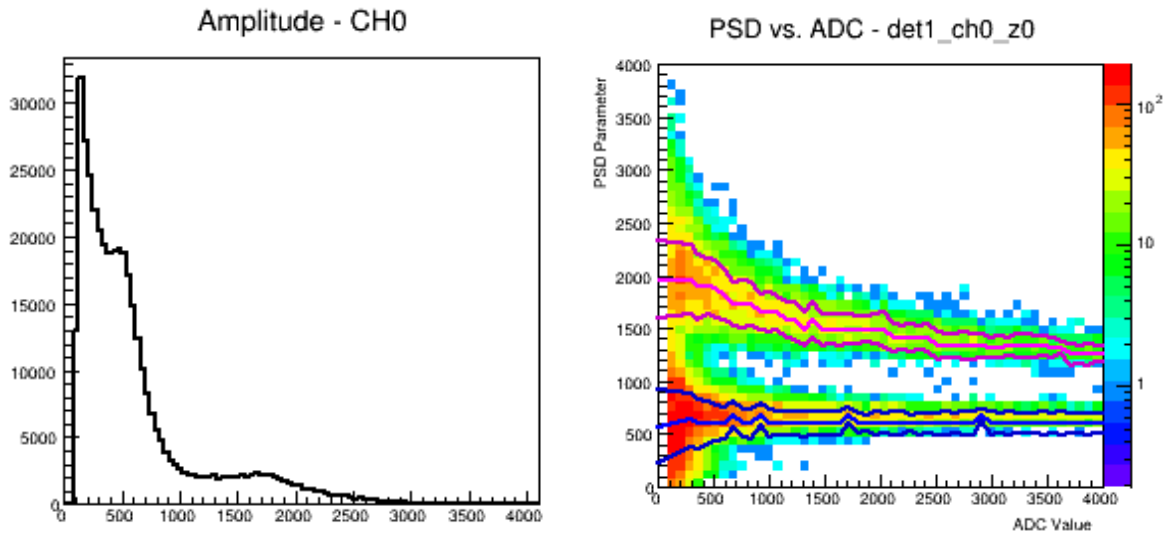

Figure 4.4. On the left, the measured peaks for a Na-22 source are used to convert to electron-equivalent energy. Right: The neutron band (pink) and gamma band (blue) are measured to select neutrons only.

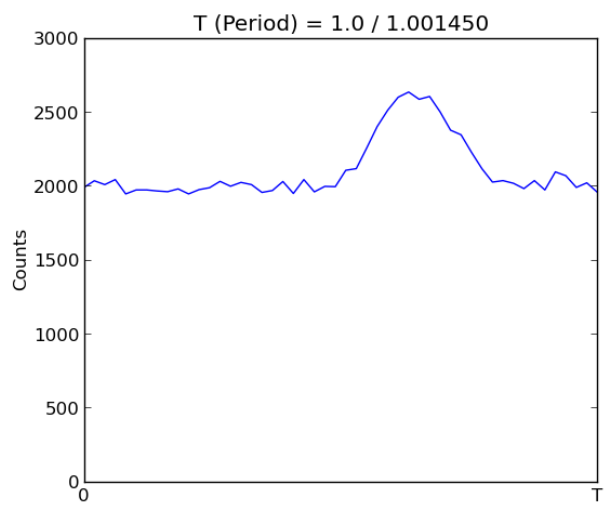

Figure 4.5. The number of neutrons for an hour-long run as a function of the bubble period. A contrast of 30% is measured

to enable easy re-use of existing Sandia developed data acquisition and analysis code, which provided an interface with the VME based hardware and implemented useful simulation and imaging algorithms, as discussed in Chap. 3. The control and collection program code linked directly to and depended on OpenCV to manipulate the video frames, as in the Python case above, but also as a means to interface with the USB camera in (mostly) real time.

The data analysis program used to process the real 1-D bubble and detector data was derived directly from code written for Chap. 3 system simulations. The mechanisms for simulating the bubble patterns and propagation and corresponding detector responses were replaced by mechanisms to introduce the real bubble and detector observation. The mechanisms for simulating the expected system response and its use in neutron source position reconstructions were retained. An aspirational goal of the project was to achieve a real-time analysis display, and this was well within grasp of the programming approach given the coding preparations made. The combined simulation and analysis programs were constructed in a way to analyze fake bubble and detector data in selectably sized chunks to mimic real-time data delivery. Also, the time-intensive process of computing the expected system response for all possible bubble masks for a given imaging scenario was designed to be carried out once, the results being stored in a manner conducive to speedy lookup of subsets applicable to processing any given real time data chunk. Ultimately, real-time display was not pursued to its end, relying instead on a ROOT file constructed for use in the real time scenario for data archiving as the connection between the data collection and analysis programs.

USB camera

While the choice of a $20 USB camera and free software to interface to it was expedient in terms of time and money, user control over camera exposure settings and frame timing were forfeit. Because of the automatic exposure control of the camera the performance of the simplified bubble detection technique described above was at the mercy of the lighting of the bubbles and background scene within the camera field of view. To better mitigate exposure variations, instead of using a fixed baseline with which to compare the frame by frame horizontal region-of-interest (ROI) slice averages, a time-weighted average baseline was computed that adapted automatically to overall changes in pixel values caused by the automatic variations in the camera's internal settings. At the same time the three color channels were combined into a single gray-scale channel for no particularly good reasons other than bubble detection performance changed little and the gray-scale channel could be recorded in the data file with one third the bits. With the addition of a cheap fluorescent tube light placed directly behind the bubble tube from the point of view of the camera and application of layers of white printer paper in between light and bubble tube for attenuation as needed, combined with adequate illumination of the visible room background, a sufficient degree of contrast between bubble and liquid could be established in the camera's pixel data upon which the simple bubble detection algorithm worked well. Figure 4.6 shows what the bubbles look like visually when backlit by the fluorescent lamp, as well as text information, bubble ROI box and aiming line placed upon the video frame. Figure 4.7 shows real-time

Figure 4.6. Photo of PC screen showing an entire USB cam frame and the text information, ROI box and aiming line placed on it using OpenCV functions.

analysis of the bubble ROI with the moving average baseline in black, the live ROI slice averages in gray (peaks are bubbles, troughs are liquid) and a simple bipolar thresholding comparing the two in red. Zero on the x axis corresponds to the top of the ROI and 500 the bottom. The y axis depicts the 8-bit gray-scale value of the baseline and live traces and arbitrarily selected values to depict the bi-polar state of the threshold comparison. After similar data as depicted in Fig. 4.7 was written and read from a ROOT data file, the top plot in Fig. 4.8 reiterates that data with the moving average baseline in red, the live ROI slice averages in green and the simple bipolar threshold comparison in blue. The bottom plot in Fig. 4.8 shows a simple transformation of the upper high resolution bipolar trace into an analysis resolution on/off mask vector

Non-determinism with respect to frame, or even pixel, timing was tougher to quantify and actively mitigate and will be covered with a literally hand-waving discussion. When the "live" camera images were displayed directly to the screen, there was a noticeable lag

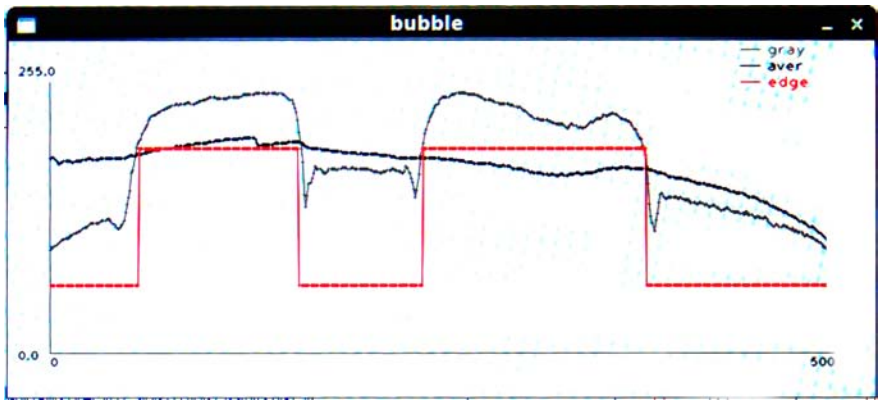

Figure 4.7. Photo of PC screen showing the real-time analysis of the bubble ROI.

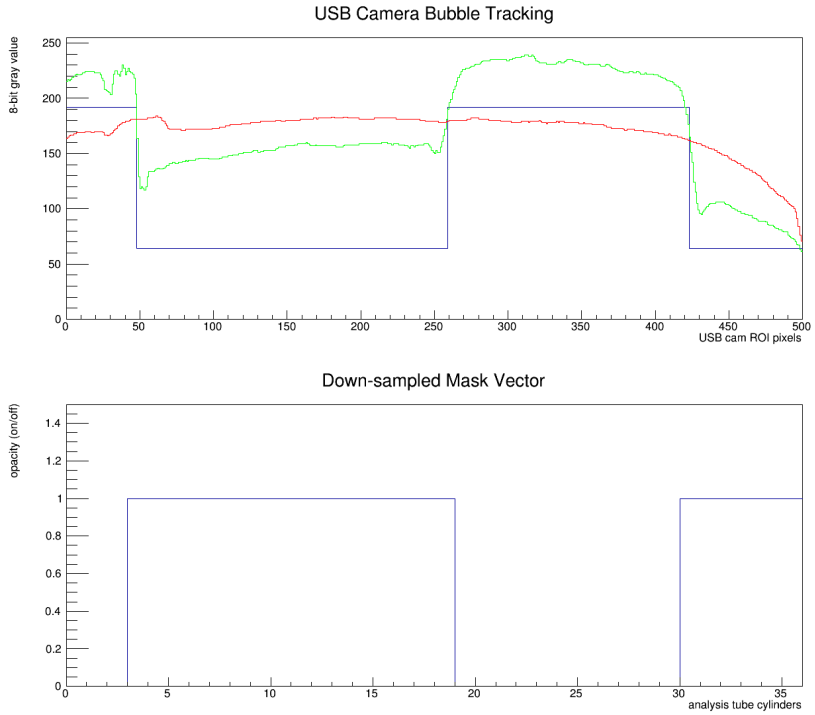

Figure 4.8. Full USB camera resolution bubble tracking data (top) and the same down-sampled, inverted and aligned to create mask vector used by source position reconstructor (bottom).

between seeing motion, of say a waving hand, in the real world and its corresponding motion in the video display. This lag applied at least at the frame level. But also by moving a straight item such as a pencil at a uniform speed—not so slow to not see the effect or so fast to be very blurred—the item's image would be curved revealing that even between pixels in a single frame there was a noticeable difference in the moments captured. This effect was dramatically more pronounced in the higher resolution USB camera that was tried and not nearly so bad in the lower resolution camera that ultimately was used. This pronounced pixel-to-pixel timing difference is plausibly associated with that camera designer's choice of a so-called "rolling" shutter rather than the other common alternative, the so-called "global" shutter. In addition to these two effects, when continuously streaming frames the display would occasionally freeze for roughly a second or so. What happened to the frames that would have been delivered otherwise during the freeze is unknown. This is related to our complete ignorance as to what truly causes a frame to be captured in the camera—the recognizance of the camera itself, or the act of a USB request for a frame? Another occasionally confounding issue was revealed when "free" running the frame acquisition at the speed determined by calling the OpenCV frame grabbing function as rapidly as possible. The frame rate achieved varied from program run to program run, never exceeding the standard NTSC TV rate of 30 frames per second but sometimes only managing 10 frames per second.

A small amount of internet research suggested that using a kilo-dollar-class digital camera designed for industrial processes would mitigate both the exposure and timing issues encountered with the cheap cameras plus open up the option of hardware based image processing in the camera itself. However, a judgment was made that none of the bad behaviors of the cheap cameras were bad enough to require a better camera to at least demonstrate the basic viability of camera based live bubble tracking. Aided by some luck, it turned out that the slow and/or variable free-run frame rate problem somehow cured itself, and all data runs enjoyed a frame rate averaged over the run of 29.5 frames per second. Figure 4.9 plots the inter-frame time of a typical run. The statistics box reports 38 overflows, which are probably frame-freeze events. Since there were 17k frames total in the run, we surmised frame freeze was not particularly impactful. A bi-modality is evident. It is not clear this was associated with bad effects, but conceivably it was a confounding factor in the spread of reconstructed source positions.

Neutron detector setup

The introduction of the new data collection system required a recalibration of the neutron detector gain. Arising from experimenter inattention to detail there are differences from the previous settings and analysis methods. Figure 4.10 (right) serves the equivalent function of Fig. 4.4 (left). The red trace shows the ^{137}Cs 662 keV Compton "edge" located roughly at 2500 in raw ADC value of the peak (i.e. mimimum) pulse value relative to the pedestal value of roughly 4000. Figure 4.10 (left) shows that this span of 1500 ADC units corresponds roughly to 500 on the arbitrarily scaled analyzed (i.e. sliding window filter) pulse amplitude

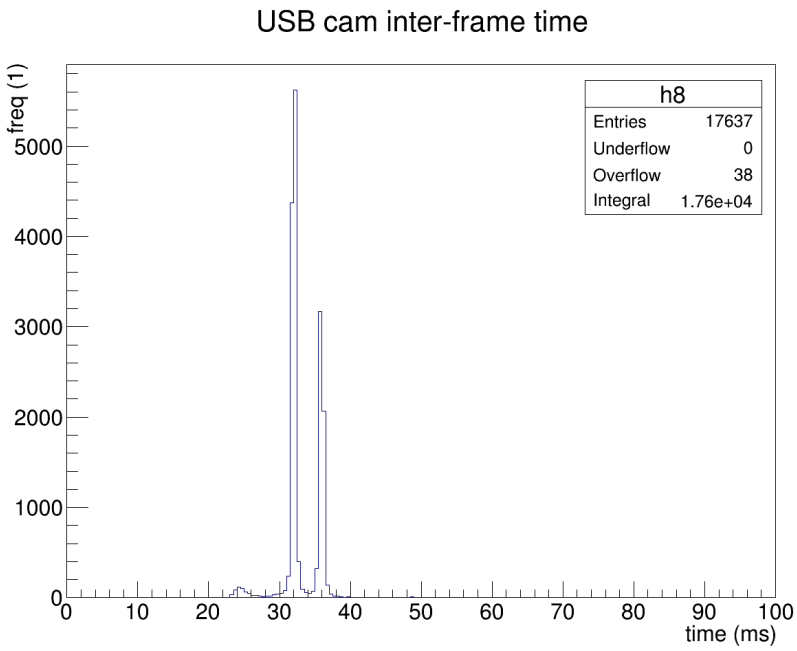

Figure 4.9. Histogram of USB camera inter-frame time as measured by high-precision CPU timer.

axis used in this and subsequent amplitude vs. pulse shape plots. Note that the pulse shape axis is also arbitrarily scaled. The green box indicates a much cruder neutron cut region than that previously used. Figure 4.11 shows the amplitude vs. pulse shape response to a neutron source showing the additional population of events to be found within the cut region. Note that the rhino horn-like upturn of the bands at higher amplitudes in Fig. 4.10 and Fig. 4.11 is most certainly due to clipping of the pulse peaks by the ADC because of the poorly chosen electrical operating point. Speaking of which, the detector photomultiplier tube was biased at -1770 V.

Arduino setup

The Arduino program was modified to allow on-the-fly adjustment of parameters via the serial interface conveyed via its USB connection. The parameters were operation mode, air value pulse period and duty cycle. The modes of operation were periodic and random. The first attempt at a random mode selected only the duty cycle on a pulse-by-pulse basis uniformly over a range of 20-90%. As will be seen in the reconstruction results from data taken using this mode, this method retained the basic periodicity defined by the period parameter. While this was an error in one respect, it proved the basic correctness of the overall experimental system's operation. The second attempt at randomizing the bubble pattern sets both the on and off interval values independently and uniformly over a range

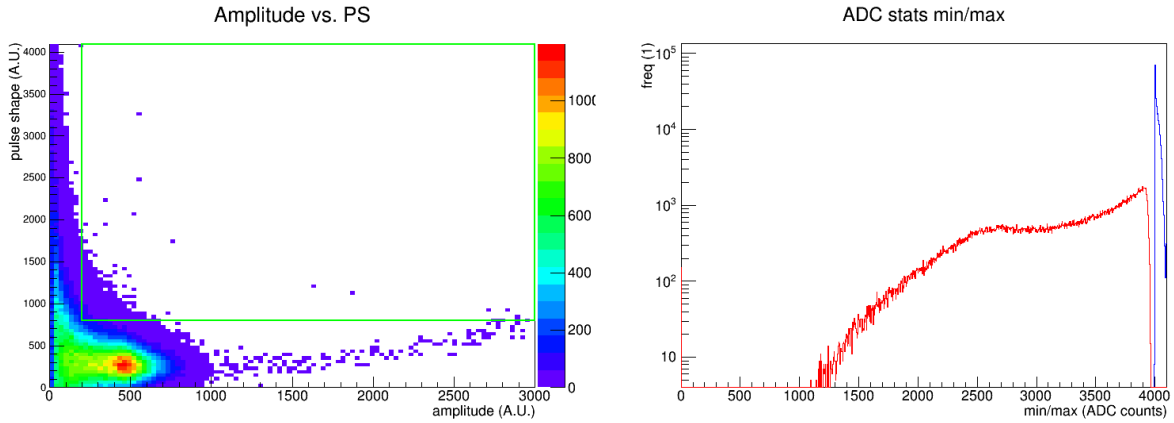

Figure 4.10. Calibration using a ^{137}Cs source. Left: amplitude vs. pulse shape. Right: minimum and maximum ADC values.

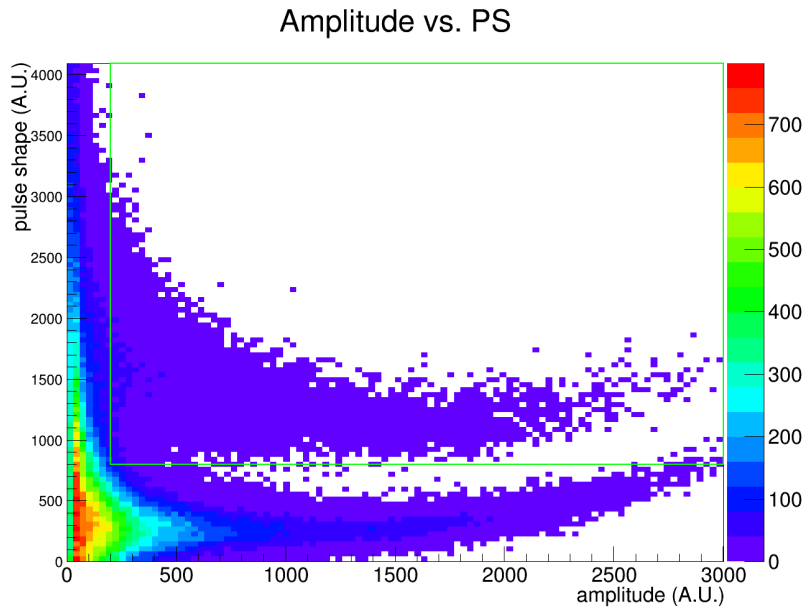

Figure 4.11. Neutron source amplitude vs. pulse shape response.

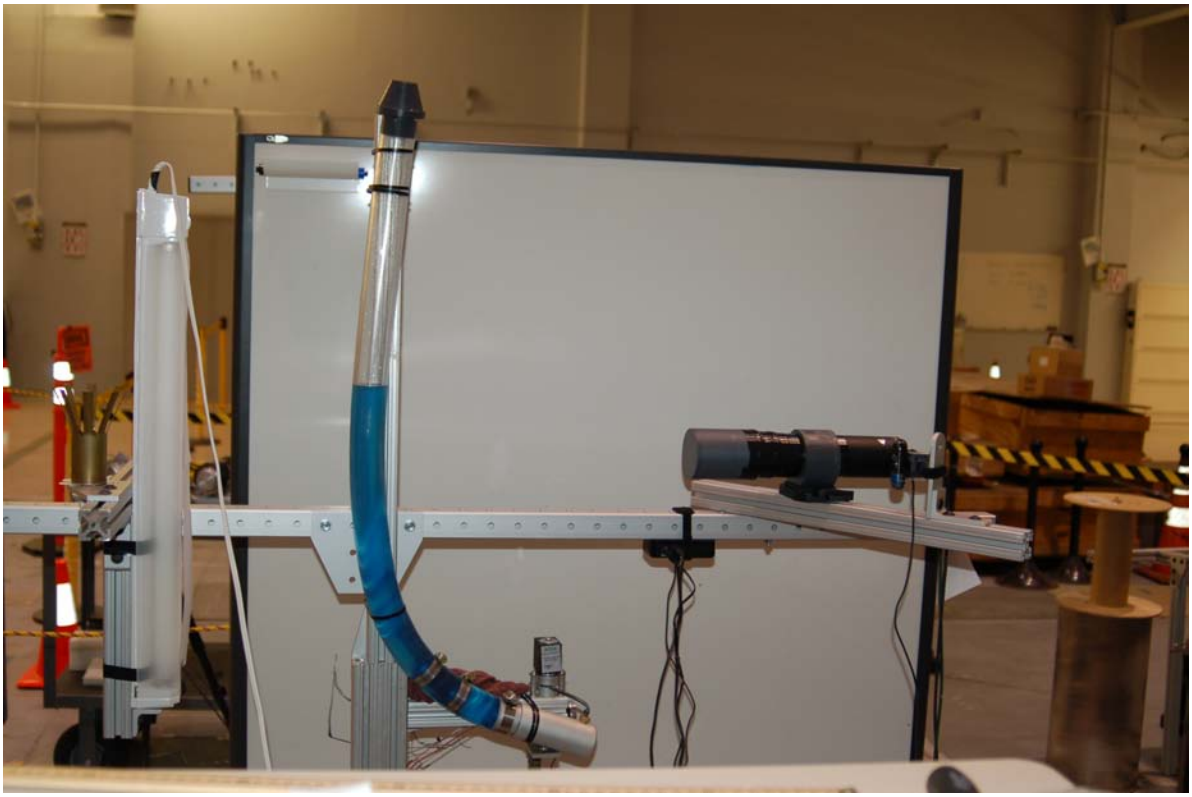

Figure 4.12. Data run 00 experimental configuration.

of 20-200% of the period parameter. As will be seen in the reconstruction results from data taken using this mode, the resulting bubble patterns exhibited a greater and perhaps more importantly uniform independence over the possible source positions.

Data collection run 00

In the debut experiment for the revamped data collection system the relationship of the source, tube and detector were arranged as seen in Fig. 4.12 in which a greater separation of the elements is used. The black cable ties were pushed out of the bubble ROI, since their presence was easily detected and artifacts in the bubble tracking resulted. The bubble tube's shape relaxed accordingly to unquantified effect. Also added was the cross beam upon which the detector and USB camera (on the right) and fluorescent light and source holder (on the left) were mounted so that if the entire apparatus was moved the relative position of the elements would remain fixed.

Keep in mind when reading thru the discussions in this and the next section that interpretations offered to support what the data reveals may not have been available before

the data that is presented after these bright ideas are discussed was taken. For example, the idea to compute and inspect the response map inner product occurred to us in order to explain periodicity in the reconstruction results even though there was no obvious need to do so after viewing the reconstruction results from the periodic bubble data alone.

Figures 4.13 and 4.14 show two runs using a periodic bubble pattern with a period of 0.75 s. The run of Fig. 4.13 had no source present and reconstruction estimates "hot spots" in a periodic pattern. That that is what one might expect can be gathered from studying the lower right plot, which shows the inner products of the response map where each horizontal z-slice is considered as a vector composed of coefficients along that slice from all frames. The idea here is that each such product between vectors reveals to what extent the vectors are correlated to each other, or in other words how non-orthogonal they are to each other. As expected the products of each vector with itself forms the 45° "spine" from lower left to upper right. If any vector is chosen and its products with other vectors are inspected it is obvious that there is a spatial periodicity in which vectors a distance of roughly 25 cm away yield a product that is nearly the same as the product of the vector with itself. Naturally, when the MLEM process is run with such a response map as input, it will weight possible sources in locations corresponding to these correlated directions nearly equally because there is no basis upon which to differentiate the true direction. Why in the no-source case the pattern is centered on $z = 0$ is not completely obvious. But a guess is that since the speed of a bubble past any given point in the tube is dependent on whether a new bubble is being injected at that time and since the bubble injection is periodic the effective open fraction for each position along the tube varies periodically also. And by chance one of the sections of tube that had a high open fraction happened to be centered around $z = 0$, and it follows the other high open fractions sections are spaced periodically around it. Explicitly computing the open fraction as function of z would be a useful exercise, but absent that, an inspection of the lower left plot showing a view zoomed in on a portion of the cumulative response map reveals that indeed there is a higher weight corresponding to the open phases at $z = 0$ and also at positions equally spaced on either side of it.

With Fig. 4.14 an AmBe source is placed at $z = 0$. The reconstructed position is obviously not at $z = 0$. However, it is clearly the case that more radiation is being detected and the possible source positions notwithstanding the bubble pattern periodicity are much narrower.

Figures 4.15 and 4.16 show two runs using a "random" bubble pattern—with a period of 0.75 s. As discussed in the Arduino section the first attempt at randomizing the bubble pattern was not entirely successful. These figures show the measurements demonstrating this failure. As with the periodic bubble pattern, a look at the response map inner product plot shows that there is a significant spatially periodic correlation between z-slice vectors, and the resulting MLEM reconstructed source positions have this same periodicity. The random bubble attempt without-source run shows the periodicity in the position reconstruction, with numerous artifact similar to the without-source periodic run. The random with-source run shows an increased overall detector response coincident with a suppression of all but three peaks, which are also shifted somewhat in the negative direction from the true position as with the with-source periodic run.

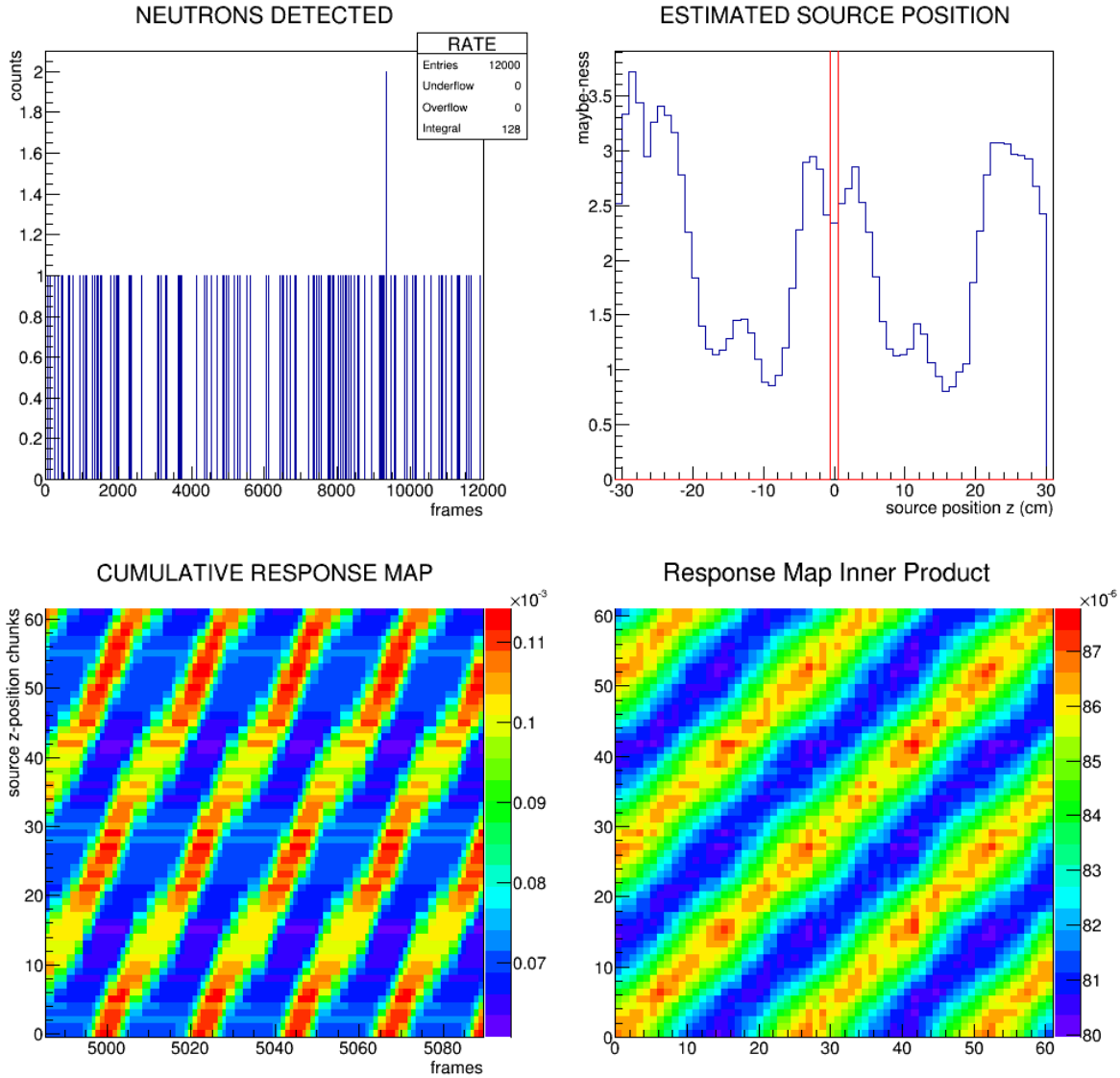

Figure 4.13. Periodic bubbles, no source.

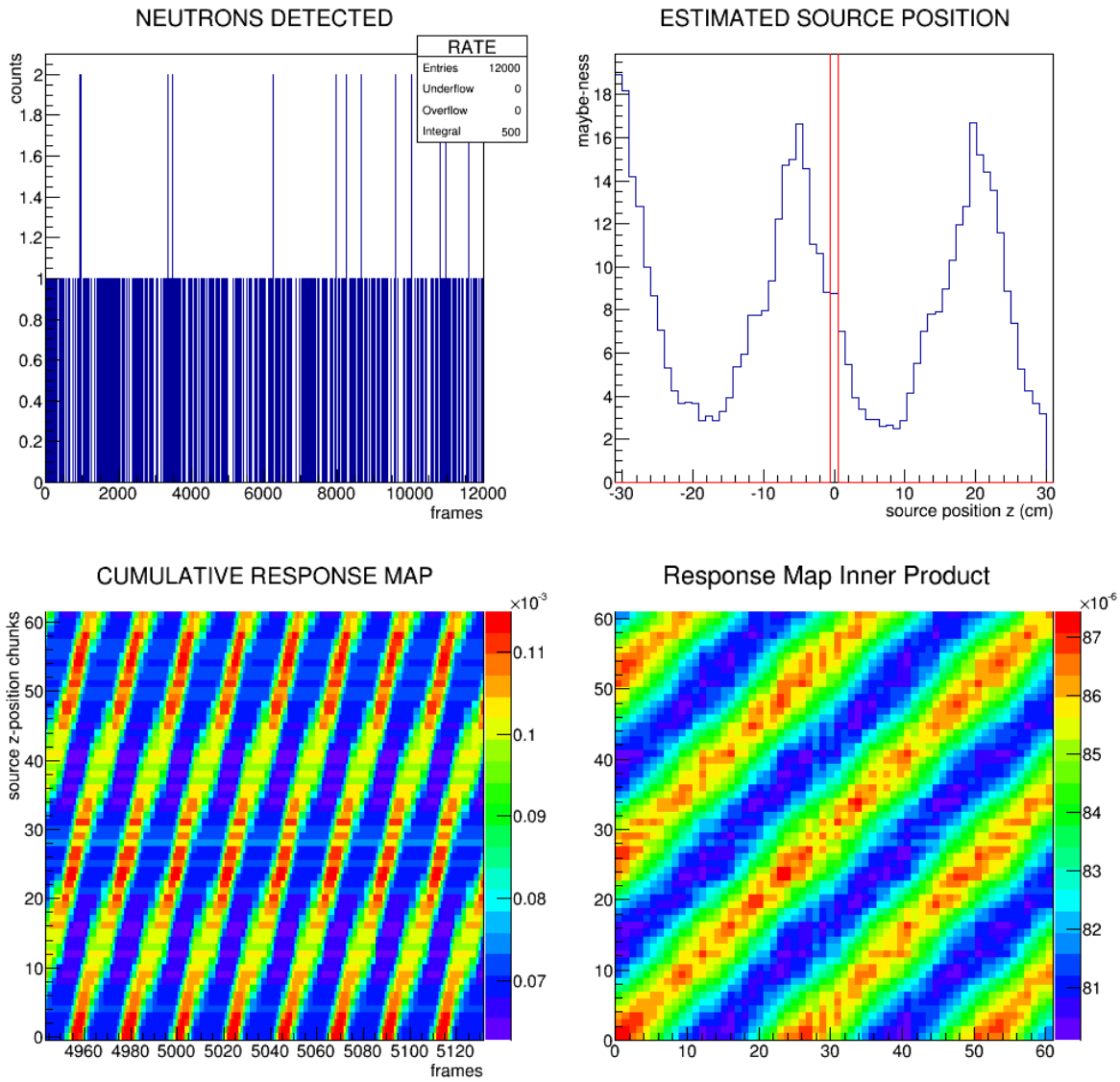

Figure 4.14. Periodic bubbles, AmBe source, $z = 0$ cm.

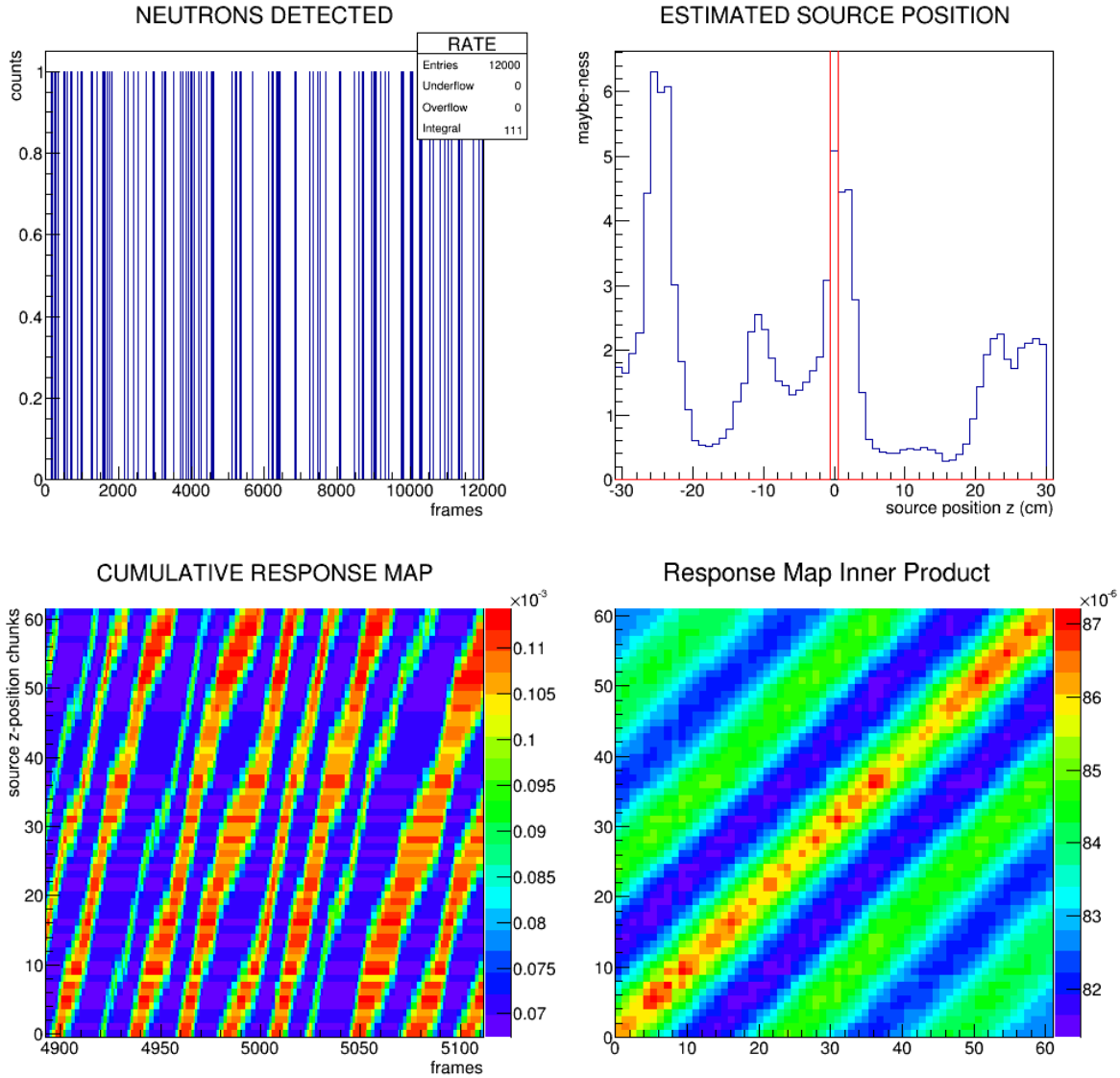

Figure 4.15. Semi-random bubbles, no source.

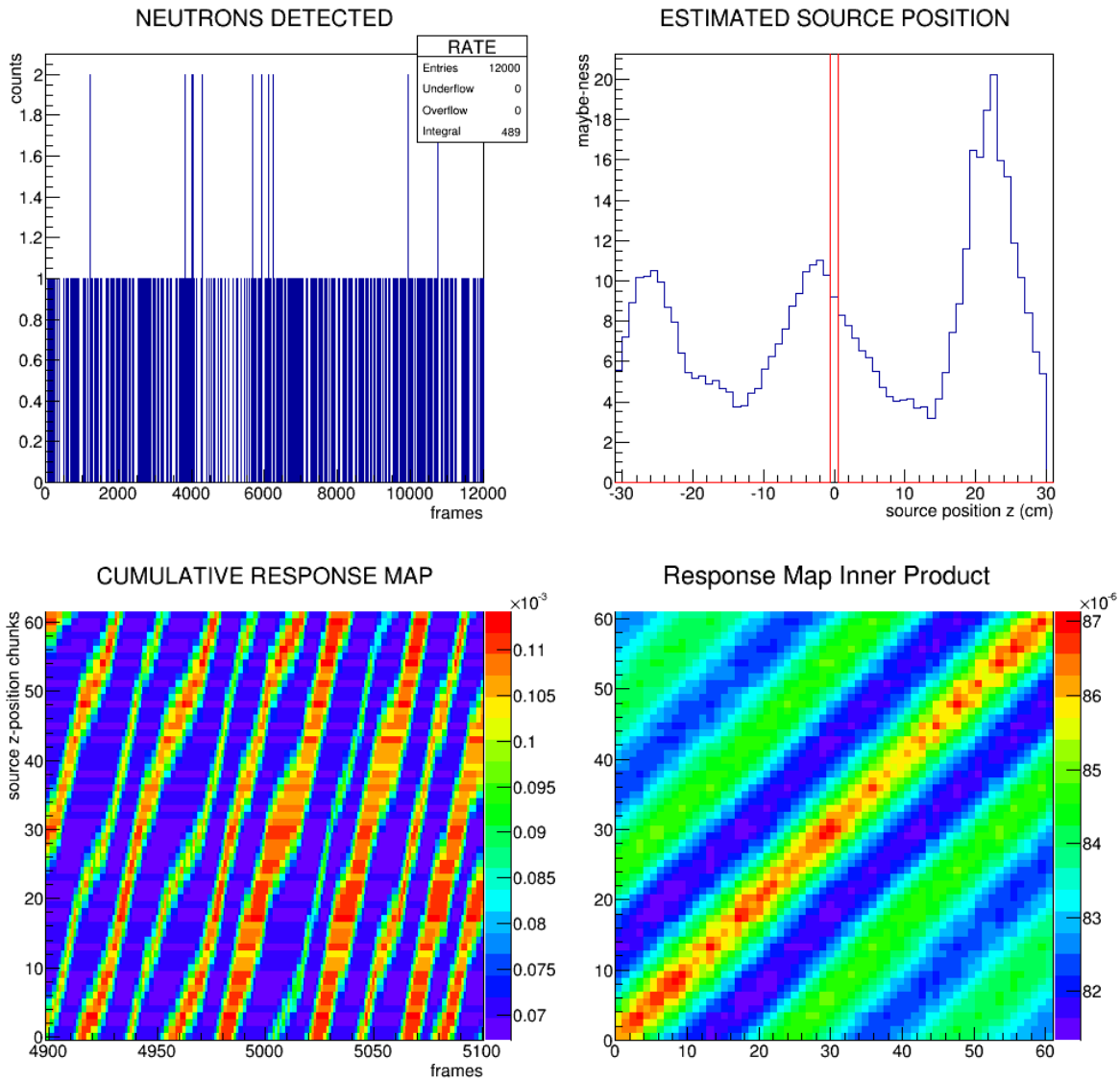

Figure 4.16. Semi-random bubbles, AmBe source, $z = 0$ cm.

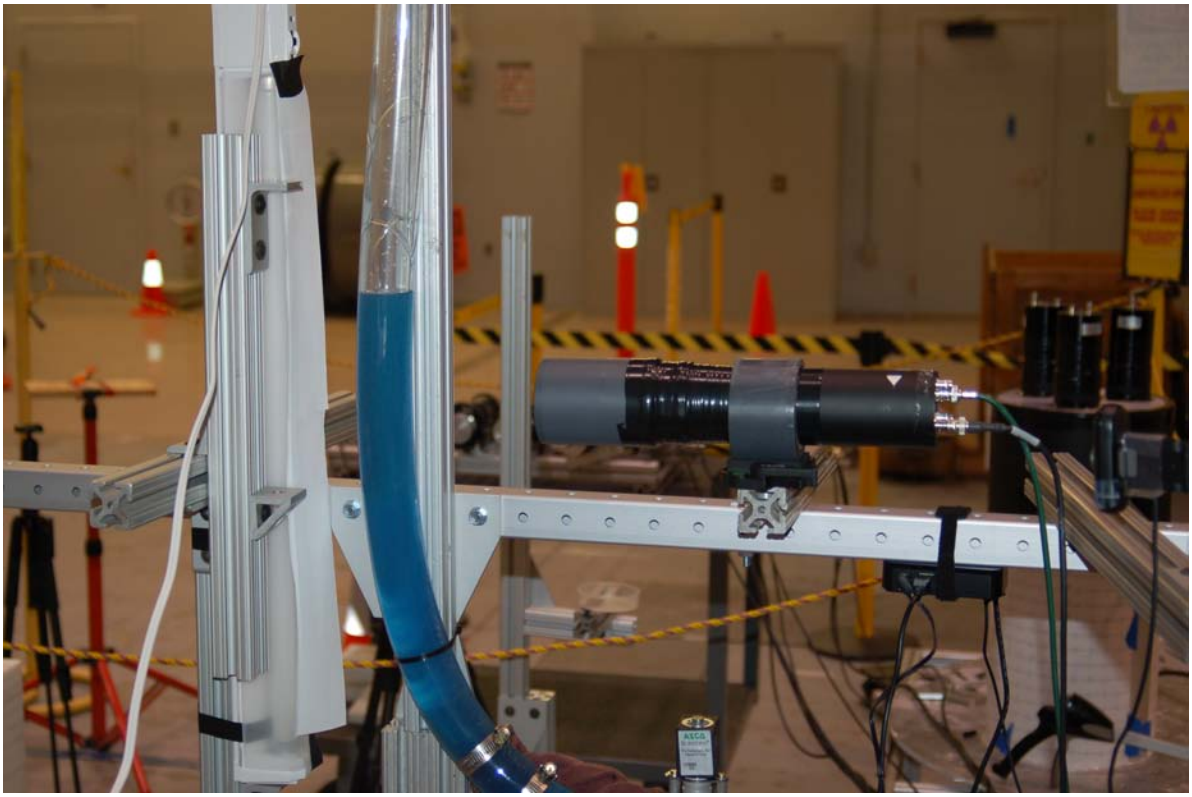

Figure 4.17. Data run 01 experimental configuration.

In the Arduino update follow on experiment for the revamped data collection system the relationship of the source, tube and detector were arranged using the compact separation of the original experimental setup.

To confirm that the new Arduino random bubble pattern generator had addressed the problem that was discovered in the previous data sets, a series of three runs were done with the neutron source at three different positions. Figure 4.18 shows a similar quad-plot to those in the previous section. Inspection of the response map inner product plot reveals that indeed the new randomizing method removes the periodic correlations between the z-slice vectors. This also appears to have the desired effect in the MLEM position reconstruction results.

Figure 4.19 shows plots of only the source position estimates of the three known source positions carried out using 2000 MLEM iterations, rather than the lower number used in the plots presented so far.

The next set of runs was taken to begin to look at the ability to resolve multiple sources. Figure 4.20 shows the result using a ^{252}Cf source and an AmBe source with roughly 1/3 the neutron rate together. Because of the compact spacing of setup and the z positions chosen for the sources, the stronger ^{252}Cf source was closer and viewed more directly thru the bubble

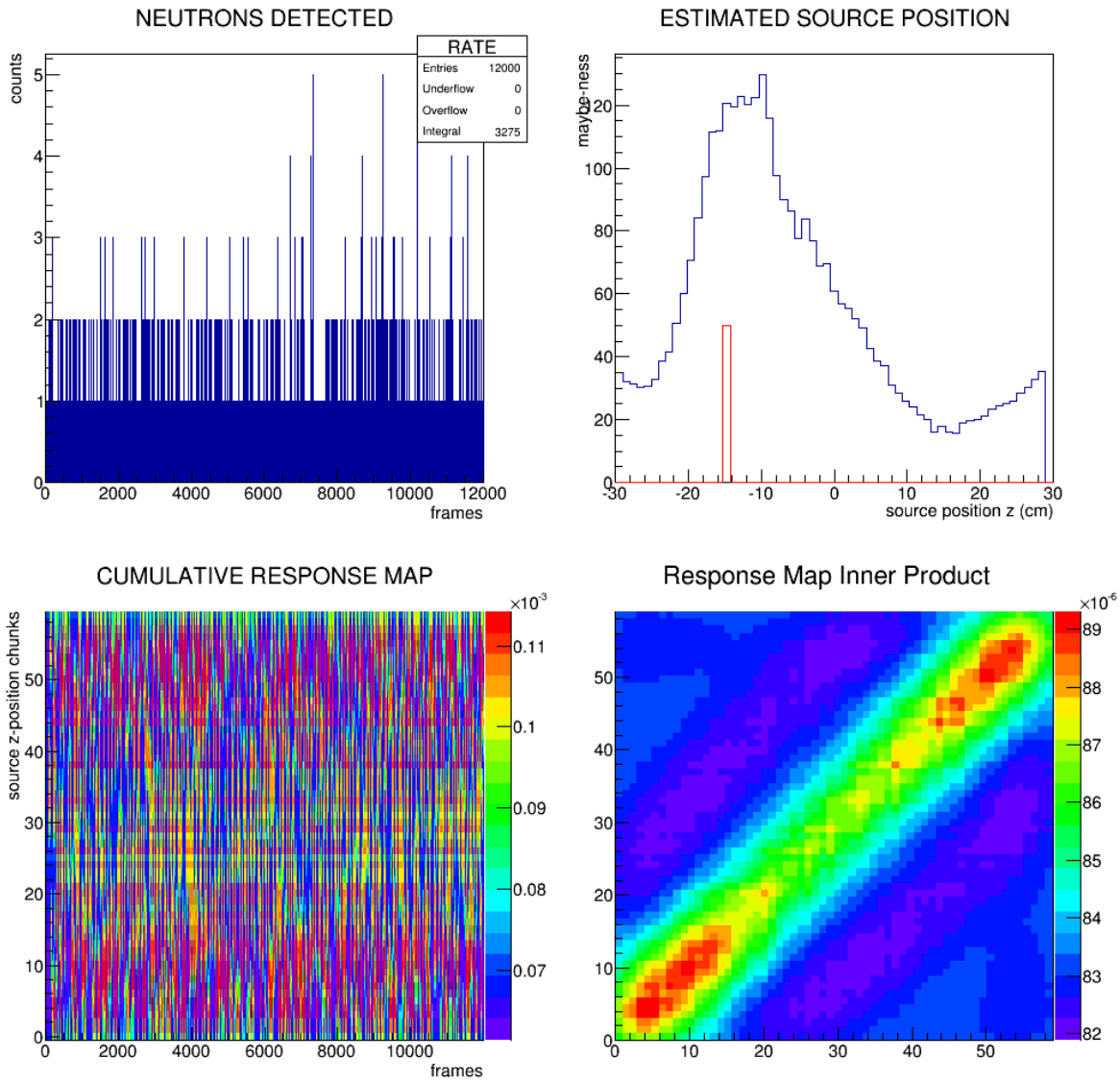

Figure 4.18. Random bubbles, AmBe source, $z = -15$ cm.

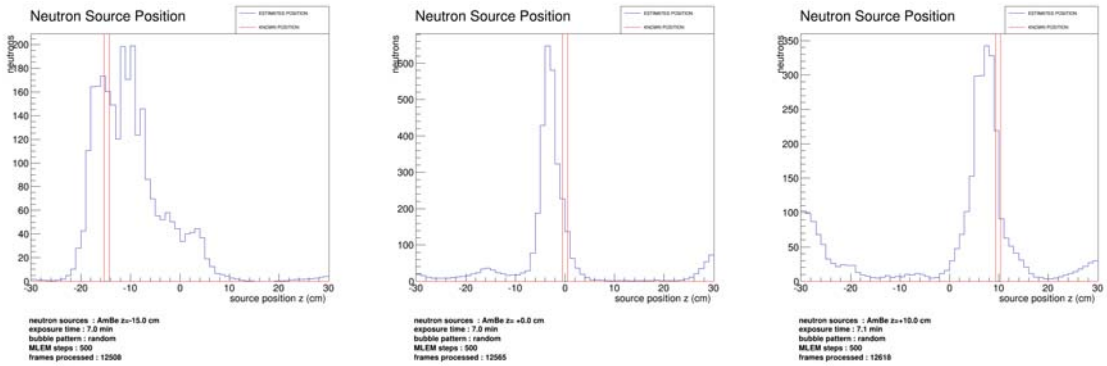

Figure 4.19. AmBe source, $z = -15$ cm (left), $z = 0$ cm (center), $z = +10$ cm (right); 7 min.

tube than the AmBe source. An estimate of the relative difference in detected neutrons expected because of this geometrical effect was roughly a factor of 1.25 in favor of the ^{252}Cf source. As can be seen in the position reconstruction, the AmBe source is essentially not to be found. What happened in this case remains a bit mysterious, since this case was not repeated to confirm that the result was repeatable. The runs presented next use sources of equal strengths or placed the weaker source at the position that is closer to the detector.

The run shown in Figure 19 did not alter the geometry of the setup from Figure 18, but replaced the AmBe source with a ^{252}Cf source of equal strength to the other ^{252}Cf source. MLEM discovered a source at the position it was previously challenged to find one and close to where a source was expected. The resolution of the other ^{252}Cf source was much degraded.

The run shown in Fig. 4.22 retains the same two ^{252}Cf sources, but swaps the z-position offsets of each source about $z = 0$.

Figure 4.23 shows what a doubling of the run time to 10 min from 5 min does while maintaining all other parameters from Fig. 4.22.

To further investigate if extending the run time continued to improve the reconstruction resolution, two 60 min runs were acquired. Figure 4.24 shows results for two equal-strength ^{252}Cf sources, and Fig. 4.25 shows the result for a return to the AmBe/^{252}Cf source combination from the run of Fig. 4.20.

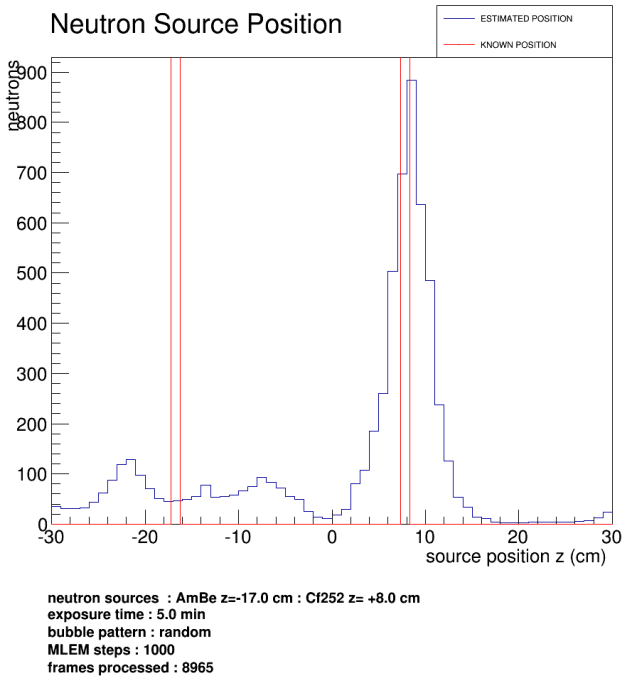

Figure 4.20. Random bubbles, AmBe and ^{252}Cf sources, 5 min.

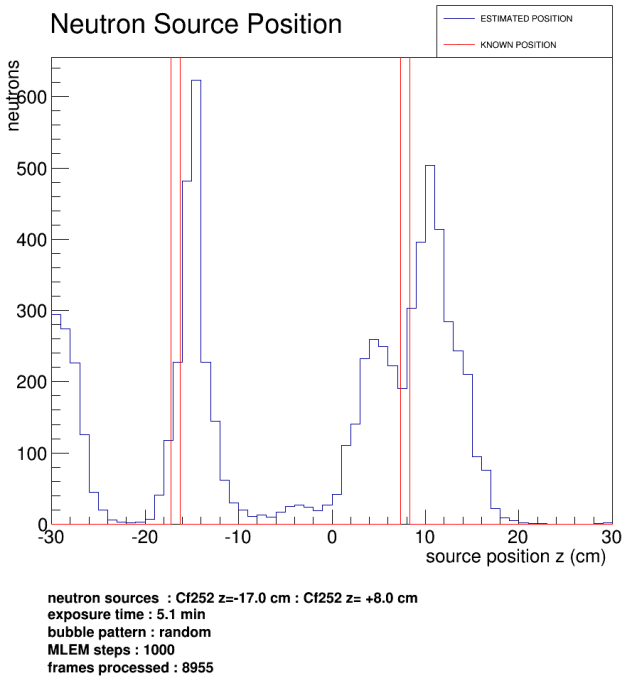

Figure 4.21. Two ^{252}Cf sources, 5 min.

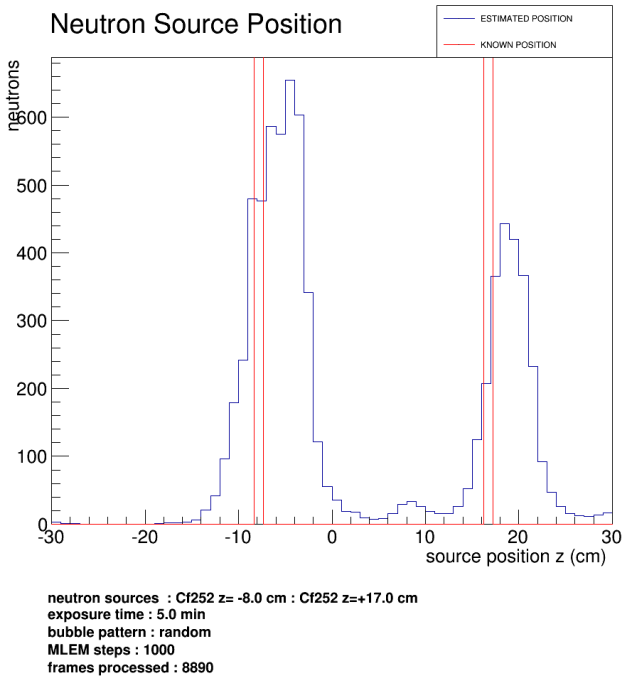

Figure 4.22. Two ^{252}Cf sources, 5 min.

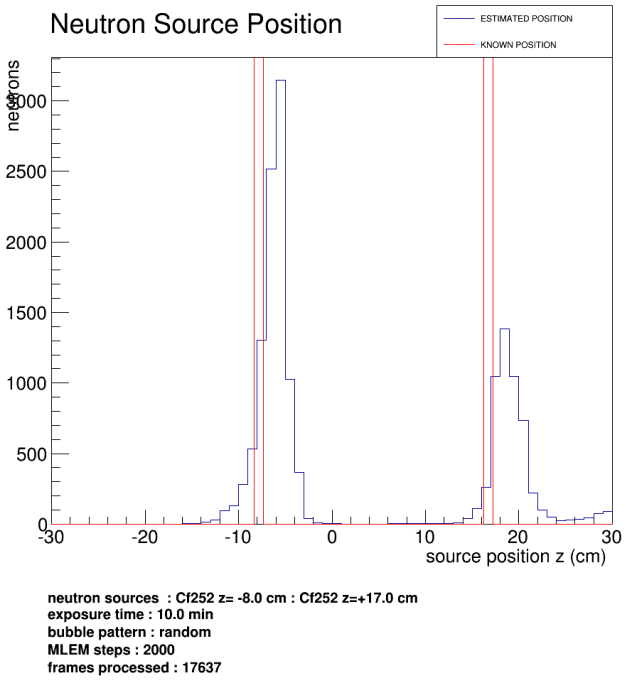

Figure 4.23. Two ^{252}Cf sources, 10 min.

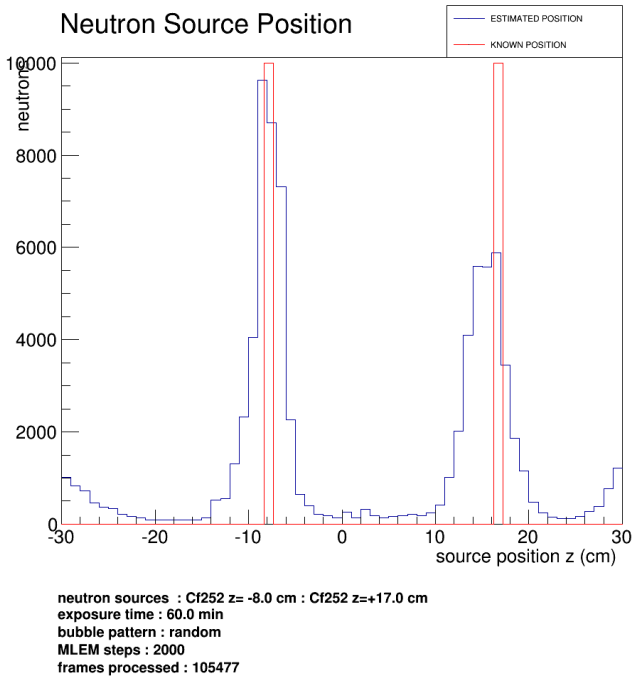

Figure 4.24. Two ^{252}Cf sources, 60 min.

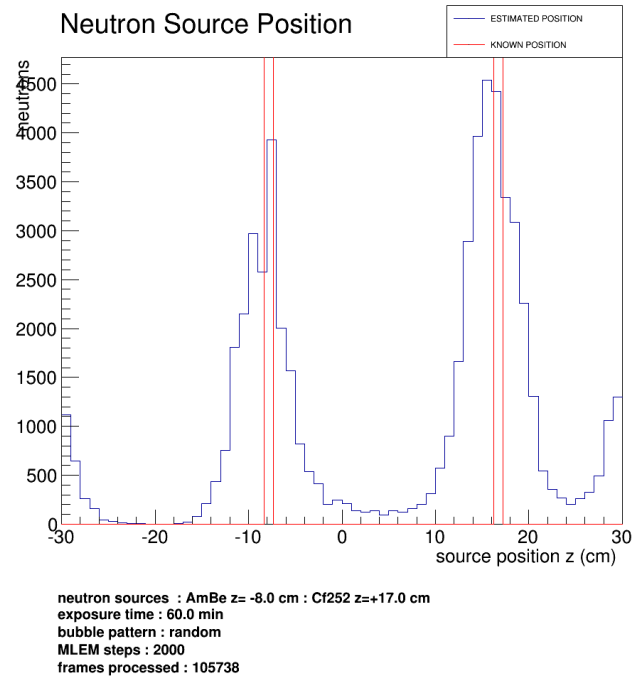

Figure 4.25. AmBe and ^{252}Cf sources, 60 min.

Chapter 5

Conclusion

The goal of this one-year project was to determine the feasibility of building bubble masks for neutron time-encoded imaging, and identify any limitations on their design or performance. We have successfully demonstrated controlled introduction and propagation of bubbles through a tube of viscous hydrogenous liquid in a pattern relevant for time-encoded imaging of fast neutrons. We developed a technique for tracking bubble positions in real time and methods to reconstruct a source distribution from acquired neutron rate data. Results from a simple experimental setup provide a demonstration of the concept, and give us confidence in simulation results. The simulation was then used to extrapolate beyond the experimental results to explore the potential performance of a large-scale imaging system based on bubble masks.

Two major limitations of the bubble mask technique were identified. The first is the challenge of achieving a high mask contrast, which would require tubes (and therefore bubbles) with large cross-sectional area, and ideally a rectangular shape. The second is the inherent correlations among the response vectors of nearby source positions, due to the motion of the bubbles through the tubes. Low mask contrast and non-ideal orthogonality both contribute to slower resolving times, or the need for more statistics for a given detection threshold or image resolution.

Advantages of the bubble mask technique include the length of the encoding pattern, which is limited only by the length of the acquisition, in contrast to fixed moving masks, which must be cyclical with some finite length. In addition, the ability to respond to observations by changing the mask pattern (adaptive encoding) has potential to improve resolving times and open up a new class of algorithms for source detection and imaging.

Future work on this concept should focus on addressing the limitations described here, either by further investigation in the bubble technique, or in related methods with similar flexibility and adaptability.

References

[1] Peter Marleau, James Brennan, Erik Brubaker, Mark Gerling, Aaron Nowack, Patricia Schuster, and John Steele. Time encoded fast neutron/gamma imager for large standoff SNM detection. In *2011 IEEE Nuclear Science Symposium Conference Record*, pages 591–595. IEEE, October 2011.

[2] E. E. Fenimore and T. M. Cannon. Coded aperture imaging with uniformly redundant arrays. *Applied Optics*, 17(3):337, February 1978.

[3] L A Shepp and Y Vardi. Maximum likelihood reconstruction for emission tomography. *IEEE transactions on medical imaging*, 1(2):113–22, 1982.

[4] G. Bradski. The OpenCV Library. *Dr. Dobb's Journal of Software Tools*, 2000.

DISTRIBUTION:

1	MS 0899	Technical Library, 8944 (electronic copy)
1	MS 0359	D. Chavez, LDRD Office, 1911

Sandia National Laboratories